RWTH AACHEN

RHEINISCH-WESTFÄLISCHE TECHNISCHE HOCHSCHULE AACHEN

Institut für Mathematik

Energetics and dynamics of global integrals modeling interaction between stiff filaments

by

Philipp Reiter
Dieter Felix
Heiko von der Mosel
Wolfgang Alt

Report No. **21** 2008

April 2008

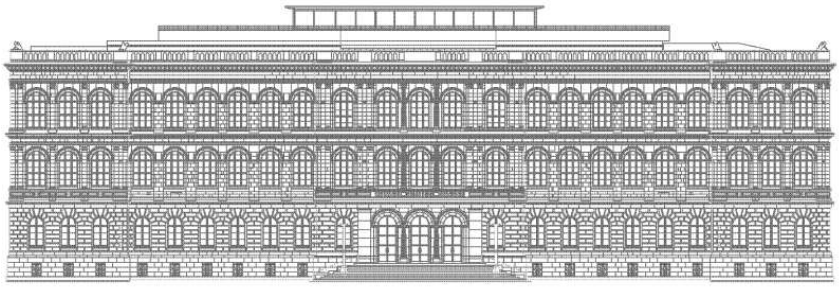

Institute for Mathematics, RWTH Aachen University

Templergraben 55, D-52062 Aachen
Germany

Energetics and dynamics of global integrals modeling interaction between stiff filaments

Philipp Reiter, Dieter Felix, Heiko von der Mosel, Wolfgang Alt

April 21, 2008

Abstract

The attractive and spacing interaction between pairs of filaments via cross-linkers, e.g. myosin dimers connecting actin filaments, is modeled by global integral kernels for negative binding energies between two intersecting stiff and long rods in a (projected) 2-dimensional situation, for simplicity. Whereas maxima of the global energy functional represent intersection angles of 'minimal contact' between the filaments, minima are approached for energy values tending to $-\infty$, representing the two degenerate states of parallel and anti-parallel filament alignment. Standard differential equations of negative gradient flow for such energy functionals show convergence of solutions to one of these degenerate equilibria in finite time, thus called 'super-stable' states.

By considering energy variations under virtual rotation or translation of one filament with respect to the other, integral kernels for the resulting local forces parallel and orthogonal to the filament are obtained. For the special modeling situation that these variations only activate 'spring forces' in direction of the cross-links, explicit formulas for total torque and translational forces are given and calculated for typical examples. Again, the two degenerate alignment states are locally 'super-stable' equilibria of the assumed over-damped dynamics, but also other stable states of orthogonal arrangement and different asymptotic behavior can occur.

These phenomena become apparent if stochastic perturbations of the local force kernels are implemented as additive Gaussian noise induced by the cross-link binding process with appropriate scaling. Then global filament dynamics is described by a certain type of degenerate stochastic differential equations yielding asymptotic stationary processes around the alignment states, which have generalized, namely bimodal Gaussian distributions. Moreover, stochastic simulations reveal characteristic sliding behavior as it is observed for myosin-mediated interaction between actin filaments. Finally, the forgoing explicit and asymptotic analysis as well as numerical simulations are extended to the more realistic modeling situation with filaments of finite length.

Keywords

Actin filaments · Polymer cross-linking · Myosin dimers · Interaction energy · Knot energies · Filament alignment · Torque · Stochastic differential equations · Generalized Gauss distributions

1 Introduction

Contact avoidance of a closed curve Γ in 3-dimensional space (like a cyclic polymer, for example, certain modified DNA strands) can be modeled by defining a global knot energy. According to [17], Def. 1.1, a real-valued functional on the space of knots is called a *knot energy*, if it is bounded from below and *self-repulsive*, i. e. blows up on sequences of embedded curves converging to a curve with a self-intersection. A large family of knot energies may be represented by global integrals of the form

$$E_\Gamma = \int_\Gamma \int_\Gamma H_{rep}\left(\gamma(s) - \gamma(\tilde{s}), \gamma'(s), \gamma'(\tilde{s})\right) \mu(\tilde{s}, s)\,. \tag{1}$$

Here $\gamma:\ I \to \Gamma \subset \mathbb{R}^3$ denotes a suitable curve parametrization with arc length coordinate $s \in I := L \cdot \mathbb{S}^1$, such that $|\gamma'(s)| = 1$ and L is the curve length. Moreover, μ describes a certain measure on $I \times I$ as, for example, the simple product measure $d\tilde{s} \cdot ds$. The positive integral kernel, H_{rep}, describes the repulsive energy between points $\gamma(s)$ and $\gamma(\tilde{s})$ distant along the curve (with $s \neq \tilde{s}$), growing to infinity when these two points approach each other. Thus, the global knot energy E_Γ models *mutual repulsion* between different parts of the curve. Minimization of such energy functionals may lead to simple circles or, depending on the knot class, to so-called 'ideal knots', which represent states of maximal 'distance' or minimal 'contact' between curve parts ([16], [22], [21]). Though existence and regularity of minimizers have been proven for certain classes of knot energies ([5], [19], [6], [3], [23] and [20]), analytical treatment and a thorough numerical simulation of corresponding dynamical gradient flow systems are rare, see [7], [13], [4].

When considering the contrary case of *mutual attraction* between two, not necessarily closed curves Γ and $\widetilde{\Gamma}$, the obvious idea is to just reverse the sign in the energy integral (1) and define $H = -H_{rep}$ as the integral kernel of a corresponding global *interaction energy*

$$E = E_{\Gamma,\widetilde{\Gamma}} = \int_\Gamma \int_{\widetilde{\Gamma}} H\left(\gamma(s) - \tilde{\gamma}(\tilde{s}), \gamma'(s), \tilde{\gamma}'(\tilde{s})\right) \mu(\tilde{s}, s)\,. \tag{2}$$

However, under the analogous conditions mentioned above for the repulsive kernels, minimization of this global interaction energy will occur for $E \to -\infty$, namely if the two curves tend to contact each other, so that locally the integrand $H(z, \theta, \tilde{\theta})$ grows towards infinitely large negative values for a vanishing distance vector $z = \gamma - \tilde{\gamma}$. For most of the used model kernels, the type of singularity that occurs in the contact limit, depends on the relation between the two local tangent vectors $\theta = \gamma'$ and $\tilde{\theta} = \tilde{\gamma}'$. In general, the dynamic properties of the resulting negative gradient flow for E in (2) would correspond to a reversed positive gradient flow for the repulsive knot energy E_{rep} in (1), and one might expect energy *blow-up* in finite time.

In the following prototypical case study we want to explain and quantitatively characterize such a blow-up behavior of global attraction energies and analyse the resulting stability properties under stochastic perturbations. For simplicity, we restrict our analysis to an idealized 2-dimensional model of long and stiff polymer filaments that stay in close contact to each other (as approximately true for actin filaments in cytoskeletal protein networks [1]). In our model, such filaments are represented by two straight (infinite) lines Γ and $\widetilde{\Gamma} \subset \mathbb{R}^2$ which (generically) always intersect: in a real 3-d situation this constellation is approximately realized for two generically non-intersecting filaments by identifying the two parallel planes, each of which contains one of the two straight filaments, under the assumption that the distance d_{min} between these planes does not change much and stays very small, so that we can consider the 2-d limit situation as $d_{min} \to 0$.

In particular, we investigate the dynamic interaction effects induced by mutual binding of certain short and relatively stiff cross-linking polymers (e.g. filamin, α-actinin or myosin dimers), which reveal thermal fluctuations at their two binding sites but have a *minimal cross-link length* $d \gg d_{min}$, thereby serving, in a twofold manner, as 'attractors' and as 'spacers' between the filaments, cf. the illustrating sketch of different cross-linking geometries in Figure 2 of [9]. Since then the integrand $H(z, \theta, \tilde{\theta})$ in model equation (2) has its support in the outer domain $\{z \in \mathbb{R}^2 : |z| = \rho \geq d\}$, the contact singularity at zero distance between corresponding binding sites (i.e. $\rho \to 0$) is avoided, but it is replaced by a new singularity appearing for *filament alignment*, namely when the two filament directions approach each other in a parallel or anti-parallel manner, i.e. for $\theta \mp \tilde{\theta} \to 0$.

In the first modeling section 2 we derive, under quite general assumptions, simple model functions for *interaction energies* between such filament pairs and present degenerate ordinary differential equations for the corresponding negative gradient flow that describes the relative rotation dynamics. By computing the variation of energy with respect to suitable variables, in section 3 we derive expressions for the forces, which are locally exerted onto one filament via different actions of cross-linkers, and supply degenerate ordinary differential equations for relative translations between two filaments.

Then, by considering a further modeling and analysis step in section 4, we discuss consistent models for stochastic force perturbations. These lead to a typical class of degenerate stochastic differential equations with additive Gaussian noise terms that have certain scaling properties near the singularity.

Finally, in section 5, we briefly discuss the more realistic model situation with stiff filaments of finite length, whereby the singularities in the dynamic differential equations are smoothed in a specific manner.

2 Measures and energies for cross-link interactions

Let us consider two (infinitely long) oriented stiff filaments Γ and $\widetilde{\Gamma}$ in $\mathbb{R}^2$ pointing into directions θ and $\tilde{\theta} \in \mathbb{S}^1$, with uniquely defined *intersection angle* $\varphi = \sphericalangle(\tilde{\theta}, \theta)$ satisfying $\cos\varphi = \theta \cdot \tilde{\theta}$ and $\sin\varphi = \theta \cdot \tilde{\theta}^{\perp}$. Here we define the orientation of $\theta^{\perp}$ by the convention $\sphericalangle(\theta, \theta^{\perp}) = \frac{\pi}{2}$. As canonical arc length parameters let us choose the signed distances s and $\tilde{s}$ from the intersection point, so that any pair of positions (potential cross-linker binding sites) on the filaments is given by the points $s\theta$ and $\tilde{s}\tilde{\theta}$, with the *contact vector* $z = s\theta - \tilde{s}\tilde{\theta}$ pointing from filament $\widetilde{\Gamma}$ towards filament Γ, see Fig. 1.

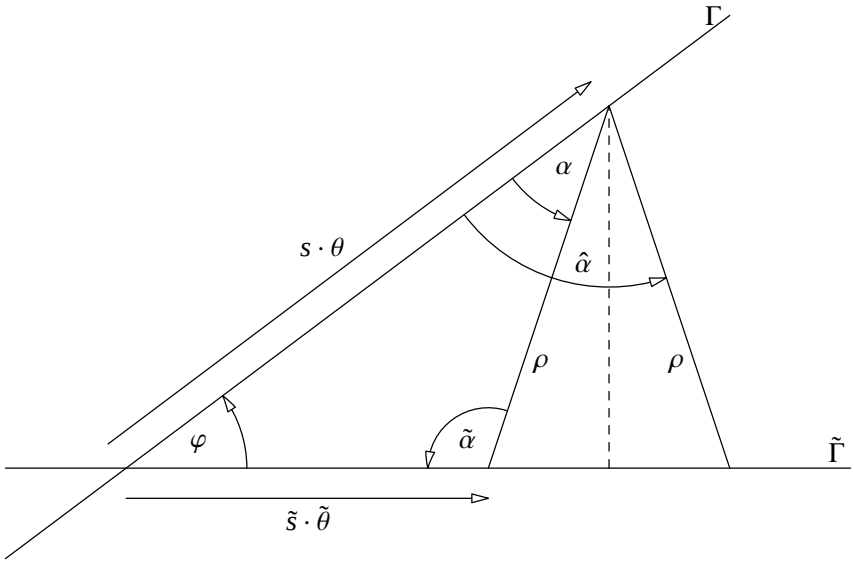

Figure 1: Sketch of two straight, infinitely long filaments Γ and $\widetilde{\Gamma}$ with intersection angle φ. At each binding site of Γ with distance s from the intersection point there can be at most two cross-link connections of length ρ to the other filament, with binding angles α or $\hat{\alpha}$ at Γ, and corresponding angles $\tilde{\alpha}$ at $\widetilde{\Gamma}$.

Since for actin filaments with typical lengths $L \succeq 1\mu m$ the binding sites for myosin are regularly spaced by $2.7\mu m$ (cf. [14]), we propose that in a justified continuum limit the binding sites for cross-linkers are continuously and uniformly distributed along both filaments and that different cross-linkers do not conflict with each other, so that we can take the simple product measure $\mu(\tilde{s}, s) = d\tilde{s} \cdot ds$ in the energy integral (2). Furthermore, assuming a quasi-stationary situation for given intersection angle $0 < \varphi < \pi$, we propose that binding probability and averaged dynamical status, i.e. the energetics of any doubly bound cross-linker only depend on the geometric configuration of its contact vector z with respect to the two filaments. More specifically, for stiff cross-linkers that cannot bend but could be elongated by thermal fluctuations to a *binding length* $\rho = |z| \geq d > 0$, the thermodynamic energy is assumed to depend only on the distance ρ and the two *binding angles* $\alpha = \sphericalangle(\theta, z)$ and $\tilde{\alpha} = \sphericalangle(z, -\tilde{\theta})$, see Fig. 1. Notice that each binding angle α at filament Γ has a

uniquely determined dual angle $\tilde{\alpha} = \pi - \varphi - \alpha$ at the other filament with the transformation properties

$$\tilde{s} = \rho \, \frac{\sin\alpha}{\sin\varphi}\,, \tag{3}$$

$$s = \rho \, \frac{\sin\tilde{\alpha}}{\sin\varphi} = \rho \, \frac{\sin(\alpha+\varphi)}{\sin\varphi}\,. \tag{4}$$

Therefore, we can reparametrize the binding position coordinates $(s,\tilde{s}) \in \Gamma \times \widetilde{\Gamma}$ by the coordinates $(\rho,\alpha) \in [d,\infty) \times (0,2\pi)$ of binding length and angle with respect to one filament, here Γ. Because the Jacobian of the transformation $(\rho,\alpha) \mapsto (s,\tilde{s})$ simply equals $J(\rho,\varphi) = \rho/\sin\varphi > 0$, this constitutes a diffeomorphism of $[d,\infty)\times[0,2\pi)$ onto the closed domain $\Omega_d = \bigcup_{\rho\geq d} C_\rho \subset \mathbb{R}^2$, where the ellipse $C_\rho = \{(s,\tilde{s}) : |s\theta - \tilde{s}\tilde{\theta}|^2 = \frac{1}{2}(1-\cos\varphi)(s+\tilde{s})^2 + \frac{1}{2}(1+\cos\varphi)(s-\tilde{s})^2 = \rho^2\}$ is 2π-periodically parametrized by the second argument α, see Fig. 2.

Notice that due to (3) and (4) the maximum norm of the ellipse satisfies $\|C_\rho\|_{\max} = \rho/\sin\varphi = J(\rho,\varphi)$, so that for $\sin\varphi \to 0$ diameter and length of the closed curve C_ρ increase in an inversely proportional manner, while the shape becomes proportionally flatter. Moreover, by inserting the Jacobian J into (2), for intersection angles $0 < \varphi < \pi$, the interaction energy E can be written as

$$E(\varphi) = \frac{1}{\sin\varphi} \int_0^{2\pi} \int_d^\infty h\,(\rho,\alpha,\pi-\varphi-\alpha)\ \rho\ d\rho\, d\alpha\,, \tag{5}$$

where the integrand is $h(\rho,\alpha,\tilde{\alpha}) = H(z,\theta,\tilde{\theta})$ with the variables satisfying the relations

$$\cos\varphi = \theta\cdot\tilde{\theta}\,; \quad z = s\theta - \tilde{s}\tilde{\theta} \tag{6}$$

$$\rho = |z|\,; \quad \zeta = z/\rho \tag{7}$$

$$\cos\alpha = \zeta\cdot\theta\,; \quad \sin\alpha = \zeta\cdot\theta^\perp \tag{8}$$

$$\cos\tilde{\alpha} = -\zeta\cdot\tilde{\theta}\,; \quad \sin\tilde{\alpha} = \zeta\cdot\tilde{\theta}^\perp\,. \tag{9}$$

Here we restrict, without loss of generality, the analysis to intersection angles $0 < \varphi < \pi$, since otherwise all the images and assertions can simply be reflected at the $\tilde{\theta}$-axis. We state the first Lemma, whose proof is straight-forward:

Lemma 1
Assume that the energy kernel $h\,(\rho,\alpha,\tilde{\alpha}) \leq 0$ in (5) is continuously differentiable and 2π-periodic in the angular variables with $h, \partial_\alpha h, \partial_{\tilde{\alpha}} h \in L^1_\rho([d,\infty)\times[0,2\pi]^2)$, where $g \in L^1_\rho$ means $\rho\cdot g \in L^1$. Further, let both integrals

$$\bar{h}_0 := -\int_0^{2\pi}\int_d^\infty h\,(\rho,\alpha,\pi-\alpha)\ \rho\, d\rho\, d\alpha \tag{10}$$

$$\bar{h}_1 := -\int_0^{2\pi}\int_d^\infty h\,(\rho,\alpha,-\alpha)\ \rho\, d\rho\, d\alpha \tag{11}$$

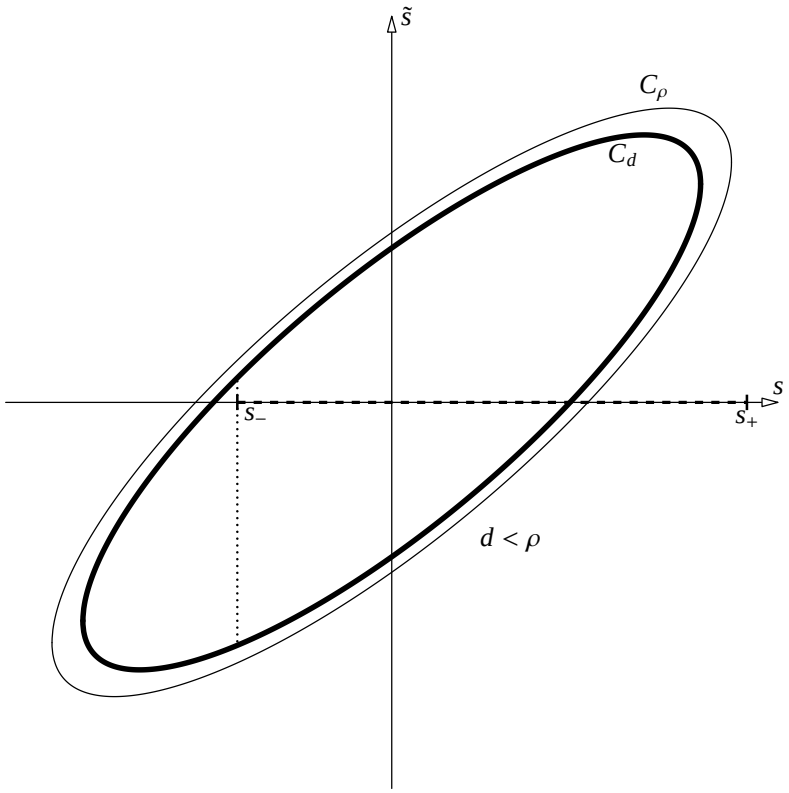

Figure 2: Representation of possible cross-linker states in the $(s, \tilde{s})$ coordinate space with C_ρ denoting all pairs of binding sites that are connected by a cross-link of length ρ. For minimal length $\rho = d$ the binding energy $k(\rho)$ in (17) has a negative jump representing the repulsive function of such cross-linkers on C_d, thereby serving as 'spacers' between the filaments. As argued in the text, the ellipses become longer and flatter (around one or the two diagonals) for $\sin\varphi \to 0$. The marked interval $[s_-, s_+]$ on the s-axis denotes the binding sites on a shorter filament Γ with finite length $L = s_+ - s_-$, intersecting a much longer filament $\widetilde{\Gamma}$, see section 5.

be positive. Then the energy functional E in (5) is continuously differentiable on the open interval $(0, \pi)$ with the following asymptotic behavior near the two *singular boundary points* $\varphi_* = 0$ and π (with $\bar{h} = \bar{h}_0$ or $\bar{h}_1$, respectively):

$$E(\varphi) = -\frac{\bar{h}}{\sin\varphi} + \mathcal{O}(1) , \tag{12}$$

$$\frac{dE(\varphi)}{d\varphi} = \frac{\bar{h}\ \cos\varphi}{\sin^2\varphi} + \mathcal{O}\left(\frac{1}{\sin\varphi}\right) . \tag{13}$$

Proposition 1 (Degenerate negative gradient flow)
According to Lemma 1 the two intersection angles $\varphi_* = 0$ and π, representing parallel and anti-parallel orientation of the two filaments, respectively, are

locally stable steady states of the *negative gradient flow* described by the standard differential equation with 'relaxation rate' $\lambda > 0$ (and with notation $\dot{\varphi}(t) = \frac{d\varphi(t)}{dt}$):

$$\dot{\varphi} = -\lambda \cdot \frac{dE(\varphi)}{d\varphi} \,. \tag{14}$$

This differential equation degenerates at $\varphi_* = 0$ and π so that the asymptotic difference $y = \sin\varphi = |\varphi - \varphi_*| + \mathcal{O}(|\varphi - \varphi_*|^3)$ fulfills

$$\dot{y} = -\lambda \bar{h} y^{-2} + \mathcal{O}(y^{-1}) \,. \tag{15}$$

Thus, these so-called 'super-stable' steady states are reached in finite positive time t_* such that

$$y(t) \sim \left[3\lambda\bar{h}(t_* - t)\right]^{\frac{1}{3}} \quad \text{for} \quad t \nearrow t_* \,. \tag{16}$$

We continue by specifying physically consistent models of the interaction energy kernel h in (5). While neglecting any small bending of a cross-linking polymer, which is approximately justified for myosin [14] and to a lesser degree also for α-actinin [24], we only consider thermal fluctuations of flexible binding chains at both ends and approximately describe the cross-link by a stochastically elongated linear spring with Hooke spring constant $\eta > 0$, but only beyond a fixed resting length d. This reflects the assumed condition that simultaneous binding of a cross-linker to both filaments cannot occur if the spring is under compression. Since energy is consumed by binding, the resulting *'half-spring'* energy induced by such a doubly bound cross-linker can be written as a function of cross-link distance ρ:

$$\begin{aligned} 0 > -\,k(\rho) &= -\,k_0 \cdot e^{-\frac{\eta}{2}[\rho-d]_+^2} \text{ for } \rho \geq d \,, \\ k(\rho) &= 0 \qquad\quad \text{for } \rho < d \,. \end{aligned} \tag{17}$$

This energy distribution does not depend on the binding angles, it vanishes for lengths $\rho < d$, jumps to the minimal value $-k_0$ at $\rho = d$ and increases to zero with increasing spring elongation $\rho \to \infty$, see Fig. 3. Then the action applied by a cross-linker onto the filaments can be expressed by the 'variational' increment $dk(\rho) = -k(\rho) \cdot \mu_f(\rho)$ in distributional sense, with a scalar force distribution μ_f given by

$$\mu_f(\rho) = \eta[\rho - d]_+ \, d\rho \;-\; \delta_{\{\rho=d\}} \,. \tag{18}$$

Whereas the first term models the attractive force by an elongated Hooke spring, the negative δ-distribution represents the repulsive action by a cross-linker at minimal length, then serving as 'spacer' between the filaments.

On the other hand, let us assume that the successive cross-link binding to one and the other filament are independent of each other and do not depend on the actual spring elongation ρ, but only on the two binding angles α and $\tilde{\alpha}$ (compare, for example, the preferred binding of α-actinin dimers to actin filaments

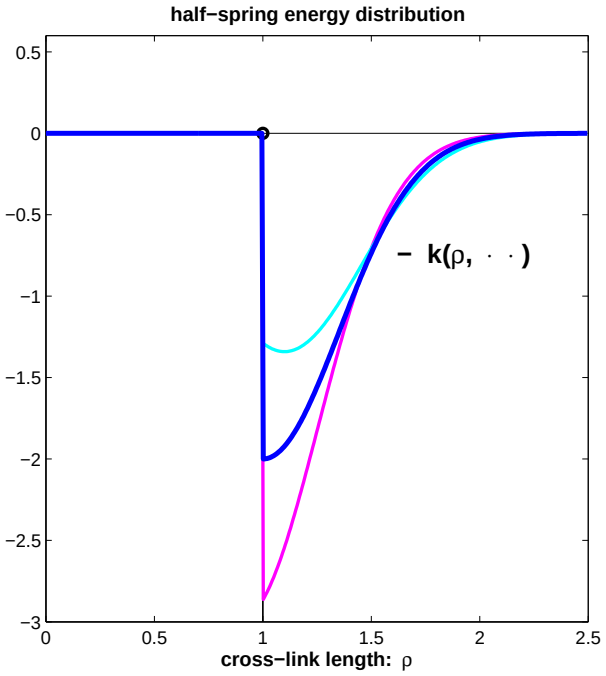

Figure 3: The negative spring energy $-k$ due to cross-link binding according to an elastic 'half-spring' model for $d = 1$. (black curve): plot of $-k(\rho)$ according to (17); (grey curves): plots of $-k(\rho, \alpha, \tilde{\alpha})$ in (27) for fixed $\hat{r} = \hat{r}(\alpha, \tilde{\alpha}) = 0.2$ yielding the lower energy curve and representing a spring in pre-tension, whereas the upper curve for $\hat{r} = -0.2$ represents pre-relaxation of the cross-link.

[24]). Then the quasi-stationary energy configuration of such a filament pair can be quantified as follows:

Example A (Cross-link forces independent of α and $\tilde{\alpha}$)
Suppose that the *energy kernel* h in (5) has a symmetric factorization

$$h\,(\rho, \alpha, \tilde{\alpha}) = -\,k(\rho, \alpha, \tilde{\alpha}) \cdot q(\alpha) \cdot q(\tilde{\alpha}) \tag{19}$$

with a 'half-spring' cross-linker energy $k(\rho, \alpha, \tilde{\alpha}) = k(\rho)$ only depending on cross-link length ρ as in (17) and an angle dependent binding strength $q(\alpha) > 0$. By defining

$$\bar{k} := \int_d^\infty k(\rho)\,\rho\,d\rho \;= \frac{k_0}{\eta}\left\{1 + d\sqrt{\frac{\eta\pi}{2}}\right\}, \tag{20}$$

the energy in (5) takes the explicit form, with $\overline{k_0} := \pi\bar{k}\frac{q_0^2}{4}$:

- *(i)* for α-independent binding, i.e. $q(\alpha) \equiv \frac{q_0}{2}$:

$$E(\varphi) = -2 \cdot \overline{k_0}\frac{1}{\sin\varphi} \tag{21}$$

- *(ii)* for $q(\alpha) = q_0 \cdot \sin^2 \alpha$, or $q(\alpha) = q_0 \cdot \cos^2 \alpha$, modeling preferred binding at angles $\alpha \approx \pm\pi/2$ or at $\alpha \approx 0$ and π, respectively (cf. Fig. 5a):

$$E(\varphi) = -\overline{k_0}\left(\frac{3}{\sin\varphi} - 2\sin\varphi\right), \tag{22}$$

$$\frac{dE(\varphi)}{d\varphi} = \overline{k_0}\,\cos\varphi\left(\frac{3}{\sin^2\varphi} + 2\right), \tag{23}$$

- *(iii)* for $q(\alpha) = q_0 \cdot \cos^2(\frac{\alpha}{2}) = \frac{q_0}{2}(1 + \cos\alpha)$, modeling preferred binding at angles $\alpha \approx 0$ and reduced binding at $\alpha \approx \pi$(cf. Fig. 5b):

$$E(\varphi) = -2 \cdot \overline{k_0}\,\frac{1 - \frac{1}{2}\cos\varphi}{\sin\varphi}, \tag{24}$$

$$\frac{dE(\varphi)}{d\varphi} = 2 \cdot \overline{k_0}\,\frac{\cos\varphi - \frac{1}{2}}{\sin^2\varphi}. \tag{25}$$

In the first two cases the energy $E(\varphi)$ on the interval $]0, \pi[$ is symmetric with maximum at $\varphi^* = \pi/2$ and with equally strong singularities of order $\frac{1}{\sin\varphi}$ at $\varphi_* = 0$ and π, see Fig. 4a, while in the last case the asymmetric energy function attains its maximum at a lower intersection angle $\varphi^* = \frac{\pi}{3}$, with a relatively stronger singularity at $\varphi_* = \pi$, see the dark curves in Fig. 4b.

Example B (Cross-link forces depending on α and $\tilde{\alpha}$)
In generalization of (17) let us assume that the 'rest length' ρ_0 of the 'half-spring' representing a cross-link of minimal length d, is not constantly equal to d but depends on the binding angles via a function $\rho_0 = d - \frac{1}{\sqrt{\eta}}\hat{r}$ with

$$\hat{r}(\alpha, \tilde{\alpha}) = \sqrt{\frac{\pi}{2}} r_0(\cos\alpha + \cos\tilde{\alpha}), \tag{26}$$

for example, see Fig. 5c. Here the two additive terms model the fact that, at each of the two cross-linker binding sites, acute local binding angles induce a pre-tension of the spring proportional to $\cos\alpha > 0$ or $\cos\tilde{\alpha} > 0$, respectively (see Fig. 3: lower curve), whereas in case of obtuse angles with negative cosine values, the same expressions model a pre-relaxation of the spring (see Fig. 3: upper curve). Indeed, for myosin monomers it is a well-known fact that their 'heavy chain' binding sites induce a pre-stretching of the myosin 'heads' after binding to an actin filament, but only in direction of the so-called 'barbed end', which here is chosen to be the direction of the vectors θ and $\tilde{\theta}$ (for myosin see [8], for general models of molecular motor cross-links see [15]).

Due to the scaling factor $1/\sqrt{\eta}$ in front of the 'relative rest length deviation' $\hat{r}$ (26), this is a dimensionless function, so that pre-tension/relaxation effects are maintained for increasingly stiff cross-linkers (i.e. spring constant $\eta \to \infty$). By substituting the rest length ρ_0 into the spring energy function (17) and multiplying it with a suitable stretching factor of order $\sqrt{\eta}$, we obtain the

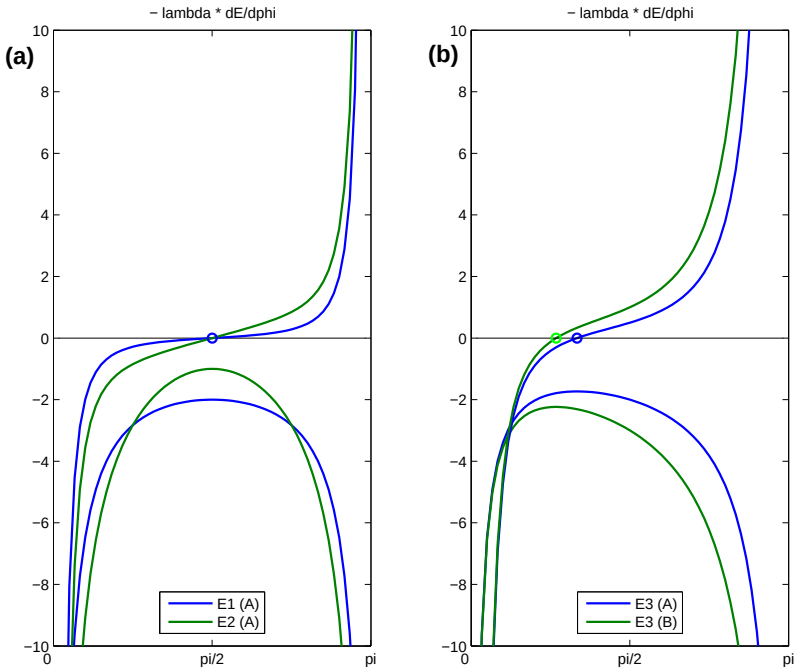

Figure 4: Plots of interaction energies $E(\varphi)$ between two filaments (the negative concave curves) and of their negative gradient flow rates $-\lambda \cdot E'(\varphi)$ (the monotone curves) according to (a) eqs. (21) in Example A(i) and (22) in Example A(ii); to (b) eqs. (24) in Example A(iii) and (34) in Example B(iii).

following (absolute value of the) modified energy function

$$\begin{aligned} k_\eta(\rho,\alpha,\tilde{\alpha}) &= \sqrt{\eta}\ \kappa\ e^{2\sqrt{\frac{2}{\pi}}\hat{r}(\alpha,\tilde{\alpha})} e^{-\frac{1}{2}\left(\sqrt{\eta}[\rho-d]_+ + \hat{r}(\alpha,\tilde{\alpha})\right)^2} \text{ for } \rho \geq d\,, \qquad (27)\\ k_\eta(\rho,\alpha,\tilde{\alpha}) &= 0 \qquad \text{for } \rho < d\,. \end{aligned}$$

In fact, its integral $\hat{k}$, measuring the averaged potential energy of a single cross-link, is independent of the spring constant η:

$$\begin{aligned} \hat{k} &:= \int_d^\infty k_\eta(\rho,\bullet,\bullet)\, d\rho \\ &= \kappa e^{2\sqrt{\frac{2}{\pi}}\hat{r}} \int_0^\infty e^{-\frac{1}{2}(r+\hat{r})^2}\, dr \\ &= \sqrt{\frac{\pi}{2}}\kappa e^{2\sqrt{\frac{2}{\pi}}\hat{r}} \left(1 - \mathrm{erfc}(\hat{r})\right)\,, \qquad (28) \end{aligned}$$

with $\mathrm{erfc}(r) := \sqrt{\frac{2}{\pi}} \int_0^r \exp(-\frac{s^2}{2}) ds$ and $\mathrm{erfc}(\infty) = 1$. Whereas $\hat{k}$ only depends on the two binding angles via $\hat{r} = \hat{r}(\alpha,\tilde{\alpha})$ in (26), the total spring energy in

analogy to (20), namely

$$\begin{aligned}\overline{k_\eta} &= \int_d^\infty k_\eta(\rho,\bullet,\bullet)\,\rho\,d\rho \\ &= \left(d-\frac{\hat r}{\sqrt{\eta}}\right)\hat k+\frac{\kappa}{\sqrt{\eta}}e^{-\frac12\hat r^2+2\sqrt{\frac{2}{\pi}}\hat r}\,,\end{aligned} \tag{29}$$

also depends on η, but converges towards $d\cdot\hat k$ for $\eta\to\infty$. Thus, with the analogous definition of the kernel $h=h_\eta$ (19), the total energy functional (5) for a filament pair can in general be computed as

$$E_\eta(\varphi)=-\frac{1}{\sin\varphi}\int_0^{2\pi}\overline{k_\eta}(\alpha,\pi-\varphi-\alpha)\cdot q(\alpha)\cdot q(\pi-\varphi-\alpha)\,d\alpha\,. \tag{30}$$

However, in the limit $\eta\to\infty$ of infinitely stiff cross-linkers, the original energy distribution $k_\eta(\rho,\bullet,\bullet)\,\rho\,d\rho$ converges to the Dirac measure $d\cdot\hat k\,\delta_{\{\rho=d\}}$, so that the energy functional $E(\varphi)=E_\infty(\varphi)$ can be represented as a global integral (2) with the singular kernel

$$H(z,\theta,\tilde\theta)\mu_d(s,\tilde s)=-d\cdot\hat k(\alpha,\tilde\alpha)\cdot q(\alpha)\cdot q(\tilde\alpha)\,d\alpha\,\delta_{\{\rho=d\}}\,. \tag{31}$$

Here $\mu_d(s,\tilde s)$ describes the 1-dimensional Hausdorff measure on the quasi-elliptic curve $C_d=\{\rho=|z(s,\tilde s)|=d\}$ in the original $(s,\tilde s)$-coordinates according to (3)–(4), see also Fig. 2.

In general, calculation of $E(\varphi)$ as an explicit function of the intersection angle φ in closed form is not possible, however, by approximating the error-function erfc in (28) for small values of the pre-tension strength r_0 in (26), we obtain $e^{2\sqrt{\frac{2}{\pi}}\hat r}\,(1-\mathrm{erfc}(\hat r))=(1+2\sqrt{\frac{2}{\pi}}\hat r+\mathcal{O}(\hat r^2))(1-\sqrt{\frac{2}{\pi}}\hat r+\mathcal{O}(\hat r^2))=1+\sqrt{\frac{2}{\pi}}\hat r+\mathcal{O}(\hat r^2)$ and thus the simple approximative kernel representation

$$\hat k(\alpha,\tilde\alpha)=\sqrt{\frac{\pi}{2}}\kappa\left(1+r_0(\cos\alpha+\cos\tilde\alpha)+\mathcal{O}(r_0^2)\right)\,. \tag{32}$$

Finally, under this assumption we derive the following explicit energy formulas, which we restrict to the two cases (i) and (iii) defined in Example A:

- *(i)* for α-independent binding, i.e. $q(\alpha)\equiv\frac{q_0}{2}$:

$$E(\varphi)=-2\cdot\kappa_0\frac{d}{\sin\varphi}\,, \tag{33}$$

  with $\kappa_0:=\left(\frac{\pi}{2}\right)^{\frac32}\kappa\,\frac{q_0^2}{2}$, the same standard formula as in (21), and

- *(iii)* for $q(\alpha)=\frac{q_0}{2}(1+\cos\alpha)$, modeling preferred binding at angles $\alpha\approx0$ and reduced binding at $\alpha\approx\pi$:

$$E(\varphi) = -2\cdot\kappa_0\frac{d}{\sin\varphi}\left\{1-\frac12\cos\varphi+r_0(1-\cos\varphi)\right\}\,, \tag{34}$$

$$\frac{dE(\varphi)}{d\varphi} = 2\cdot\kappa_0\;d\;\frac{(1+r_0)\cos\varphi-(\frac12+r_0)}{\sin^2\varphi}\,. \tag{35}$$

In the last case the energy $E(\varphi)$ is again an asymmetric function on $]0,\pi[$ as in Example A(iii), attaining its maximum at an even smaller value φ_* such that $\cos\varphi_* = \frac{1}{2}\frac{1+2r_0}{1+r_0}$, which for small r_0 is $\varphi_* = \frac{\pi}{3} - \frac{r_0}{\sqrt{3}} + \mathcal{O}(r_0^2)$. See also the corresponding plots in Fig. 4b.

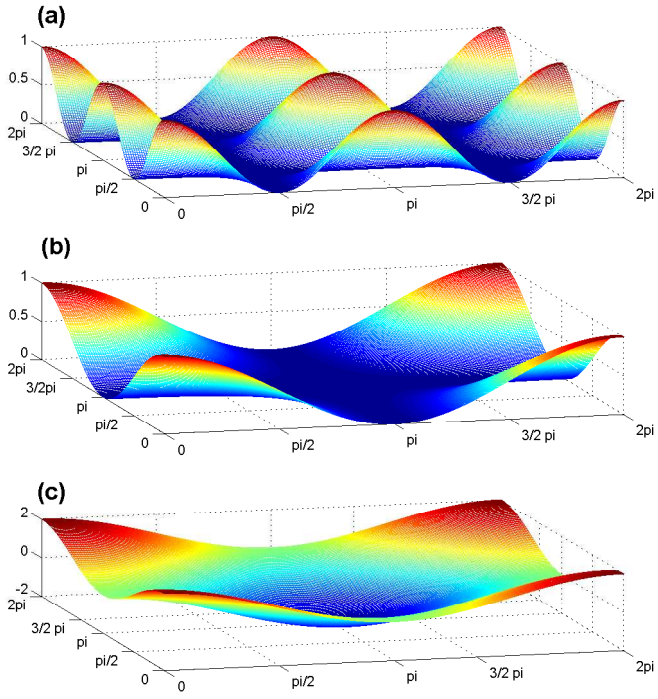

Figure 5: Symmetric model functions depending on the binding angles. Plotted over α and $\tilde{\alpha}$ are the product of binding strengths $q(\alpha)\cdot q(\tilde{\alpha})$ for (a) $q(\alpha) = q_0\cos^2\alpha$ and (b) $q(\alpha) = \frac{q_0}{2}(1+\cos\alpha)$ with $q_0 = 1$, and in (c) the rescaled deviation of cross-linker rest length from the basal value d, namely $\hat{r}(\alpha,\tilde{\alpha}) = \sqrt{\frac{\pi}{2}}r_0(\cos\alpha + \cos\tilde{\alpha})$ with $r_0 = \sqrt{\frac{2}{\pi}}$.

3 Forces and dynamics induced by cross-linkers

In order to get insight into the physical mechanisms that lead to the singular behavior described in Proposition 1 and asserted in Examples A and B, we can extract the effective forces exerted by cross-linker interactions with the aid of computing the different variations of the energy functional E in (2) and (5) under changes in the relative position between the two filaments Γ and $\widetilde{\Gamma}$. Assuming, for instance, that the latter filament is fixed, then we can consider virtual translations of the other filament Γ at a given binding position s in

two orthogonal directions ζ and $\zeta^\perp$, i.e. in direction of the cross-linker contact vector $z = \rho \cdot \zeta$, see (6)–(7), and orthogonal to it. The first variation ($\delta\zeta$) means that the cross-linker length ρ is increased, say by $d\rho$, while both binding angles α and $\tilde{\alpha}$ stay fixed. The other variation ($\delta\zeta^\perp$) induces a rotation of the cross-linker around the fixed binding site $\tilde{s}$ on $\widetilde{\Gamma}$ such that the local turn, say by $d\sigma$, of the lever (with constant length ρ) induces changes of both binding angles α and $\tilde{\alpha}$ by $d\alpha = -d\tilde{\alpha} = 1/\rho\, d\sigma$, since the sum $\alpha + \tilde{\alpha} = \pi - \varphi$ stays fixed due to pure translation of the whole filament Γ under constant φ. Thus, the force resulting from virtual spring length variations ($\delta\zeta$) is the contracting or spacing *spring force*, which in terms of the kernel h (19) can be written as

$$K_f(s,\tilde{s}) = -\,\partial_\rho h(\rho,\alpha,\tilde{\alpha}) \cdot \zeta = \partial_\rho k(\rho,\alpha,\tilde{\alpha}) \cdot q(\alpha) \cdot q(\tilde{\alpha}) \cdot \zeta\,, \tag{36}$$

where the 'unit cross-link vector' is $\zeta = \zeta_\theta(\alpha) = (\cos\alpha)\theta + (\sin\alpha)\theta^\perp$, cf. (7)–(9). On the other hand, from rotational variations ($\delta\zeta^\perp$) we obtain the sum of two *cross-link torque forces*

$$K_\omega(s,\tilde{s}) \;=\; -\frac{1}{\rho}\partial_\alpha h(\rho,\alpha,\tilde{\alpha}) \cdot \zeta^\perp\,, \tag{37}$$

$$K_{\tilde{\omega}}(s,\tilde{s}) \;=\; \frac{1}{\rho}\partial_{\tilde{\alpha}} h(\rho,\alpha,\tilde{\alpha}) \cdot \zeta^\perp\,, \tag{38}$$

so that the total force exerted by a cross-linker connection from the fixed binding site $\tilde{s}$ at $\widetilde{\Gamma}$ to the binding site s on Γ is given by the following *force kernel* $K : \Gamma \times \widetilde{\Gamma} \to \mathbb{R}^2$:

$$K = K_f + K_\omega + K_{\tilde{\omega}}\,. \tag{39}$$

Remark (Integral representation of total forces)
First, let us mention that integration over the local spring force in (36) yields, using integration by parts over ρ, an explicit expression for the total force due to contractile/spacing action of cross-linkers in terms of the integral kernel h:

$$\begin{aligned}\mathbf{K}_f := \int_\Gamma \int_{\widetilde{\Gamma}} K_f(s,\tilde{s})\; ds\, d\tilde{s} \;&=\; -\,\frac{1}{\sin\varphi}\int_0^{2\pi}\int_0^\infty \partial_\rho h(\rho,\alpha,\tilde{\alpha}) \cdot \zeta\; \rho d\rho\, d\alpha \\ &=\; \frac{1}{\sin\varphi}\int_0^{2\pi}\int_0^\infty h(\rho,\alpha,\tilde{\alpha}) \cdot \zeta\; d\rho\, d\alpha\,,\end{aligned} \tag{40}$$

where this identity also holds for Example B, even in the limiting case of infinite stiffness ($\eta \to \infty$) for the kernel in (31). Then, introducing the notation $h_\varphi(\rho,\alpha) = h(\rho,\alpha,\pi-\varphi-\alpha)$ and noticing $\partial_\alpha h_\varphi = \partial_\alpha h - \partial_{\tilde{\alpha}} h$ as well as $\zeta(\alpha) = -\partial_\alpha \zeta^\perp(\alpha)$, we conclude that the total force onto Γ vanishes:

$$\begin{aligned}\mathbf{K} \;&=\; \int_\Gamma \int_{\widetilde{\Gamma}} K(s,\tilde{s})\; ds\, d\tilde{s} \\ &=\; \frac{1}{\sin\varphi}\int_0^{2\pi}\int_d^\infty \left\{h \cdot \zeta - \partial_\alpha h_\varphi \cdot \zeta^\perp\right\}\; d\rho\, d\alpha \\ &=\; -\frac{1}{\sin\varphi}\int_d^\infty \int_0^{2\pi} \partial_\alpha (h_\varphi \cdot \zeta^\perp)\; d\alpha\, d\rho \;=\; 0\,.\end{aligned}$$

This assertion has to be true since the defining energy $E(\varphi)$ does only depend on φ and is therefore invariant under pure translations of one filament with respect to the other. Thus, the only global dynamic action on the filament pair is the *total torque* $\Omega = -\frac{\delta E}{\delta \varphi} = -E'(\varphi)$ to be computed by variation of E with respect to the intersection angle φ itself, while holding s and $\tilde{s}$ fixed. This can be computed and identified with the integral formula obtained by using the local forces in (36)–(38) and the mechanical lever laws for torque moments, with virtual rotation around the fixed intersection point ($s = \tilde{s} = 0$), yielding the following equality

$$\Omega = \int_\Gamma \int_{\tilde{\Gamma}} \Big\{ s\theta^\perp \cdot (\sigma K_f + K_{\tilde{\omega}}) + \tilde{s}\tilde{\theta}^\perp \cdot ((1-\sigma)K_f + K_\omega) \Big\}\, d\tilde{s}\, ds\,. \tag{41}$$

Here σ is an arbitrary fraction of unity, e.g. $\sigma = 1/2$, because one observes the symmetric identity

$$s\theta^\perp \cdot \zeta = \tilde{s}\tilde{\theta}^\perp \cdot \zeta = \frac{\rho}{\sin\varphi} \sin\alpha \cdot \sin\tilde{\alpha}\,. \tag{42}$$

Thus, the resulting differential equation for temporal changes in φ (see Prop. 3 below) is the negative gradient flow (14). However, the local forces appearing in the two kernels K_ω and $K_{\tilde{\omega}}$ arise from variations ($\delta\zeta^\perp$) that change the binding angles, so that in the presented energy model they can be associated to resisting 'torque' forces of cross-linkers that stay bounded to actin filaments during the variation of binding angles. Such a model (satisfying the gradient flow kinetics) could be relevant for physical situations of steadily cross-linked molecules, whereas for the biophysical situation of ongoing dissociation and re-association of cross-linking dimers (as myosin or filamin) on a *mesoscale* (of several seconds) during slow filament motion on *a macroscale* (of minutes), we have to modify the model. Since for computing the virtual forces, only variations on an even faster *microscale* (fractions of seconds) are considered, we can assume that during this short time the cross-links stay bounded. Then due to the model interpretation of the binding strengths, $q(\alpha)$ and $q(\tilde{\alpha})$, these would not change, and the only remaining variations are that of the spring energy $k(\rho, \alpha, \tilde{\alpha})$. Moreover, if we suppose that the angle-dependence of k (for the model in Example B) via the pre-tension/relaxation function $\hat{r}$ has been realized already during binding of the cross-link, then the only effective variation that remains is the one in cross-linker length ($\delta\zeta$). Thus, as local force vector kernel we can take $K = K_f$ and assume $K_\omega = K_{\tilde{\omega}} = 0$. Splitting K into its components parallel and orthogonal to the filament Γ, namely $K = K_\parallel \theta + K_\perp \theta^\perp$ and using the relations (8)–(9) as well as (42), we obtain the following explicit formulas for the *total torque* and *parallel and orthogonal force components* expressed in $(\rho, \alpha, \tilde{\alpha})$-coordinates:

Proposition 2 (Total torque and forces onto one filament)
Assume that bound cross-links only apply forces to the filaments due to elongation of their 'half-spring' but not due to bending or tilting of their binding

angles, thus $K_\omega = K_{\tilde\omega} = 0$. Then under the assumption that filament $\widetilde\Gamma$ is fixed, local variation of cross-linkers leads to the force kernel $K = K_f$ in (36) yielding the following global torque Ω and the parallel and orthogonal forces $F^\parallel = \int_\Gamma \int_{\widetilde\Gamma} K_\parallel(s,\tilde s)\; d\tilde s\; ds$ and $F^\perp = \int_\Gamma \int_{\widetilde\Gamma} K_\perp(s,\tilde s)\; d\tilde s\; ds$ onto filament Γ (again using integration by parts):

$$\begin{aligned}
\Omega &= -\frac{1}{\sin^2\varphi}\int_0^{2\pi}\int_d^\infty \partial_\rho h(\rho,\alpha,\tilde\alpha)\; \rho^2 d\rho\; \sin\alpha\sin\tilde\alpha\; d\alpha \\
&= \frac{2}{\sin^2\varphi}\int_0^{2\pi}\int_d^\infty h(\rho,\alpha,\tilde\alpha)\; \rho\; d\rho\; \sin\alpha\sin\tilde\alpha\; d\alpha \qquad (43)\\
F^\parallel &= \frac{1}{\sin\varphi}\int_0^{2\pi}\int_d^\infty h(\rho,\alpha,\tilde\alpha)\; d\rho\; \cos\alpha\; d\alpha \qquad (44)\\
F^\perp &= \frac{1}{\sin\varphi}\int_0^{2\pi}\int_d^\infty h(\rho,\alpha,\tilde\alpha)\; d\rho\; \sin\alpha\; d\alpha \qquad (45)
\end{aligned}$$

with the total translational force given by

$$\mathbf{K} = \mathbf{K}_f = F^\parallel\; \theta + F^\perp \theta^\perp\,. \qquad (46)$$

Before computing explicit expressions for Ω, $F^\parallel$ and $F^\perp$ as functions of φ in specific examples, let us write down the dynamical equations describing the resulting motion of one filament with respect to the other.

Proposition 3 (Over-damped dynamics of filament motion)
Let us assume that one filament, say $\widetilde\Gamma$, is held fixed and represented by the oriented x-axis, for instance. Then the dynamics of the other filament, Γ, under over-damping conditions (i.e. strong friction relative to inertia) is determined by the following force balance equations for the three independent types of motion (rotation, parallel and orthogonal translation), where each of them can eventually have a different friction coefficient (λ^{-1}):

$$\begin{aligned}
\frac{d\varphi}{dt} &= \lambda_{\circlearrowleft}\,\Omega\,, \qquad (47)\\
\frac{ds}{dt} &= \lambda_\parallel\; F^\parallel\,, \qquad (48)\\
\frac{ds^\perp}{dt} &= \lambda_\perp\; F^\perp\,, \qquad (49)
\end{aligned}$$

with the torque Ω the other forces defined in (43)–(45). Let us remark that for finite filaments the inverse friction coefficients λ due to Stokes formula would depend on its length L in a manner that $\lambda_\perp = 2\cdot\lambda_\parallel \sim L^{-1}$, but $\lambda_{\circlearrowleft} \sim L^{-2}$, compare section 5.
In general, the motion of Γ is completely determined by the intersection coordinate $x = R(t)$ with filament $\widetilde\Gamma$ (the x-axis), the intersection angle $\varphi = \Phi(t)$ and the signed segment length $s = S(t)$ between the intersection point $(R(t),0)$ and a freely chosen but fixed point $(X(t),Y(t))$ on filament Γ, e.g. the filament mass center, see Fig. 7d below. Thus we obtain the representation

$$X = R + S\,\cos\Phi\,, \qquad Y = S\,\sin\Phi\,, \qquad (50)$$

where the defining time-dependent variables Φ, S, R satisfy the system of differential equations (again for angles $0 < \Phi < \pi$, without restriction of generality):

$$\frac{d\Phi}{dt} = \lambda_{\circlearrowleft}\, \Omega(\Phi)\,, \tag{51}$$

$$\frac{dS}{dt} = \lambda_{\parallel}\, F^{\parallel}(\Phi) + \frac{\lambda_{\perp}}{\tan\Phi}\, F^{\perp}(\Phi)\,, \tag{52}$$

$$\frac{dR}{dt} = -\frac{\lambda_{\perp}}{\sin\Phi}\, F^{\perp}(\Phi)\,. \tag{53}$$

The last equation (53) and the second term in equation (52) arise from orthogonal shifts of filament Γ. Thus, for infinitely long filaments the 'leading' degenerate ODE (51) autonomously determines the dynamics of filament intersection angle $\Phi(t)$, whereas subsequent integration of the other two, $\Phi(t)$-dependent equations (52)–(53) yields the relative position of one filament with respect to the other. For filaments of finite length, the analogous ODE system turns out to be nonlinearly coupled in the first two variables, see section 5.

In order to characterize and visualize different types of filament dynamics for the various interaction models, we now compute the torque $\Omega(\varphi)$ as well as the force terms $F^{\parallel}(\varphi)$ and $F^{\perp}(\varphi)$ for the examples introduced in section 2:

Example A (Cross-link forces only depending on ρ)
With the conditions and definitions after eq. (20) we can state:

- *(i) and (ii)* Since in these cases the force kernel $h(\rho, \alpha, \pi - \varphi - \alpha)$ in (40) turns out to be an odd function of the periodic variable α, both integrated forces $F^{\parallel}$ and $F^{\perp}$ vanish. Thus, for these models with symmetric interaction energy $E(\varphi) = E(\pi - \varphi)$ the filament dynamics shows no translations, only rotation around the fixed intersection point. In the standard case *(i)* we obtain the torque $\Omega = -E'(\varphi)$ for the energy in (21) and, thus, a resulting negative gradient flow. On the contrary, this does not hold for *(ii)*, where in case of $q(\alpha) = q_0 \sin^2\alpha$ we have

$$\Omega(\varphi) = -\overline{k_0}\cos\varphi \left\{ \frac{5}{\sin^2\varphi} - 2 \right\}, \tag{54}$$

  and for $q(\alpha) = q_0 \cos^2\alpha$

$$\Omega(\varphi) = -\overline{k_0}\cos\varphi \left\{ \frac{1}{\sin^2\varphi} - 2 \right\}. \tag{55}$$

  Whereas in the first case the symmetric function $\Omega(\varphi)$ is monotone increasing with the unstable zero $\varphi^* = \pi/2$, in the second case this *orthogonal configuration* is a stable equilibrium state with two additional unstable zeros at $\varphi^* = \pi/2 \pm \pi/4$, see the plots in Fig. 6a.

- *(iii)* With the asymmetric binding strength $q(\alpha) = \frac{q_0}{2}(1+\cos\alpha)$ also the torque function becomes asymmetric according to (43):

$$\Omega(\varphi) = -\overline{k_0}\left\{\frac{2\cos\varphi - \frac{1}{2}}{\sin^2\varphi} + 1\right\}, \tag{56}$$

while the global forces according to (44) and (45) are

$$F^{\parallel}(\varphi) = -2\widetilde{k_\eta}\,\frac{1-\cos\varphi}{\sin\varphi}, \tag{57}$$

$$F^{\perp}(\varphi) = -2\widetilde{k_\eta}\,, \tag{58}$$

with $\widetilde{k_\eta} = \left(\frac{\pi}{2}\right)^{\frac{3}{2}} \frac{k_0}{\sqrt{\eta}}\,\frac{q_0^2}{4}$. Notice that the total orthogonal force onto the filament in (58) is just a negative constant (for $0 < \varphi < \pi$)!

Only for the last Example A(iii) the intersection point $(R, 0)$ between the moving filament and the fixed one changes due to parallel and orthogonal net forces, see Fig. 6b. Since there is a constant orthogonal 'right-shift' of the filament (to the right side with respect to its orientation vector θ) but a simultaneous parallel 'back-draw', at least for angles $\Phi > 0$, one cannot easily conclude, in which direction the filament is translocated. Therefore, we have to study the ODE-System (51)–(53), which for parameter values $\overline{k_0} = 2\widetilde{k_\eta} = 1$ (equivalent to $d + \sqrt{\frac{2}{\pi\eta}} = 1$) and inverse frictions $\lambda_{\circlearrowleft} = 1$, $\lambda_{\parallel} = \lambda$ and $\lambda_{\perp} = 2\cdot\lambda$ (all parameters and variables in dimensionless units) yields

$$\frac{d\Phi}{dt} = -\left\{\frac{2\cos\Phi - \frac{1}{2}}{\sin^2\Phi} + 1\right\}, \tag{59}$$

$$\frac{dS}{dt} = -\lambda\frac{1+\cos\Phi}{\sin\Phi}, \tag{60}$$

$$\frac{dR}{dt} = 2\cdot\lambda\frac{1}{\sin\Phi}. \tag{61}$$

According to Fig. 6b the intersection angle $\Phi(t)$ generically converges to one of the two alignment states, where with (15)–(16) we obtain the following asymptotic behavior:
At *parallel alignment*, see Fig. 7b, we have the rapid convergence $\Phi(t) \sim [t_* - t]_+^{1/3}$ in finite time, so that by $\dot{R}(t) \sim \frac{2\lambda}{\Phi(t)} \sim -\dot{S}(t)$ we obtain the corresponding convergence $R_* - R(t) \sim [t_* - t]_+^{2/3} \sim \Phi(t)^2$. Thus, the intersection point $R(t)$ increases a bit, but gets stationary at a certain value R_* even more rapidly than the intersection angle. Since on this asymptotic order the sum $(R+S)(t) \sim R_* + S_*$ is already stationary, the fixed point (marked in Fig. 7d) on the moving filament does perform an almost circular arc while approaching the fixed filament.
At *antiparallel alignment*, see Fig. 7a, we get the same asymptotic behavior for $\widetilde{\Phi(t)} = \pi - \Phi(t)$ and $R(t)$, even with a bit stronger coefficient, but now the segment length $S(t) \sim S_*$ on the moving filament is already stationary on the

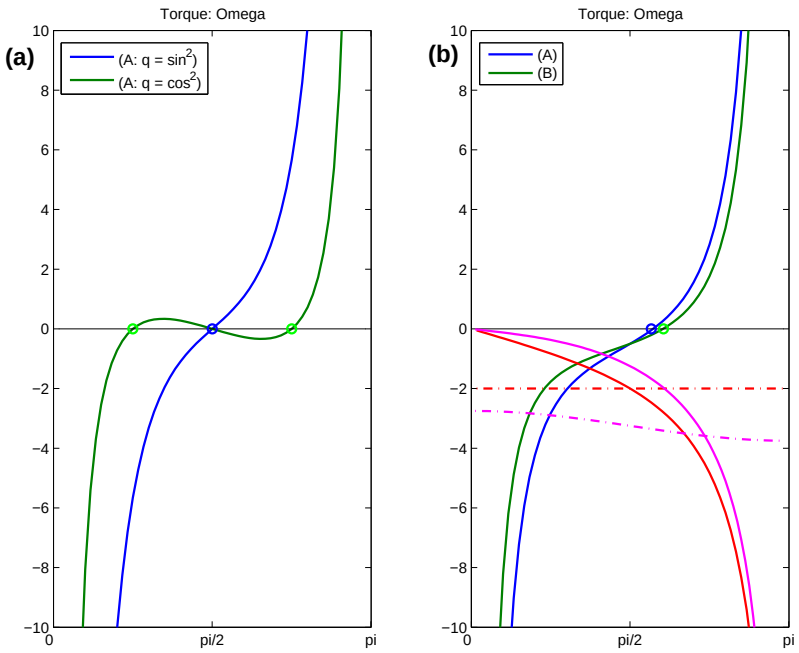

Figure 6: Plots of the φ-dependent torque between two filaments (if one is fixed) according to (a) eqs. (54) and (55) in Example A(ii) for the two indicated cross-link binding functions $q(\alpha)$: The case $(\sin^2 \alpha)$ of preferred orthogonal binding gives a torque similar to the negative gradient flow rate $-\lambda \cdot E'(\varphi)$ with the same convergence behavior as the standard function for Example A(i), see Fig. 4a, whereas the case $(\cos^2 \alpha)$ of preferred parallel binding of cross-linkers (see Fig. 5a) induces a non-monotone torque, with dynamic properties totally different from the negative gradient flow: the orthogonal filament pair configuration is an asymptotically stable state; (b) torque plots according to (56) for Example A(iii) and (65) for Example B(iii). In addition, for both examples the parallel (lined) and orthogonal (dashed) force components are plotted.

considered asymptotic order, so that the increasing intersection point 'draws' the fixed point to the right and its track is straightened to a line almost orthogonal to the fixed filament. For larger 'translation mobility' coefficient λ the fixed point is even translated to the right, meaning that the moving filament shows an asymptotic tendency to slide with respect to the fixed one (see Fig. 7c). This only happens for near antiparallel alignment, since then most of the cross-links are bound with acute angles at both ends.

This is a clear asymmetric behavior, whose importance becomes even more apparent when stochastic perturbations are considered, see section 4 below. Before doing this, we look at the deterministic dynamic behavior in the other

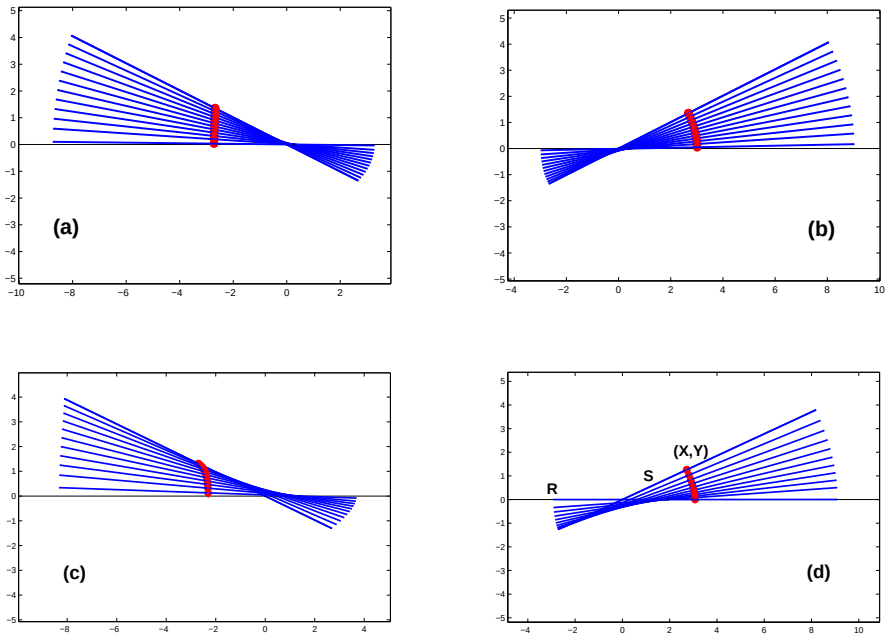

Figure 7: Plots of the filament dynamics according to the differential equations (51)–(53) for Examples A(iii) and B(iii) with the intersection angle $\Phi(t)$ converging either to the antiparallel steady state π, see (a) and (c), respectively, or to the parallel steady state 0, see (b) and (d). As inverse friction coefficient we chose: (a) and (b) $\lambda = 1$; (c) and (d) $\lambda = 3$. Drawings of the moving filament (for simplicity of finite length) are performed for time intervals with constant decrease in the intersection angle: the angular speed itself becomes infinitely rapid according to $|\dot{\Phi}(t)| \sim [t_* - t]^{2/3}$, see text for further discussion. On each filament a fixed point with coordinates (X, Y) is marked.

Example B (Cross-link forces depending on α and $\tilde{\alpha}$)
With the conditions after eq. (26), using the force representation in (40) for the singular measure (31) with the simplified force kernel (32), we can state:

- *(i)* For constant binding strength $\frac{q_0}{2}$ the force distribution kernel (for $\eta \to \infty$) is

$$K_f\, \mu_d = -\frac{d}{\sin\varphi}\sqrt{\frac{\pi}{2}}\kappa\frac{q_0^2}{4}\,(1 - r_0(\cos\alpha + \cos\tilde{\alpha}))\cdot\zeta\; d\alpha\,,$$

  so that the torque becomes

$$\Omega(\varphi) = -2\kappa_0 d\,\frac{\cos\varphi}{\sin^2\varphi} = -E'(\varphi) \tag{62}$$

and the two force components

$$F^{\parallel}(\varphi) = -\kappa_0 r_0 \frac{1-\cos\varphi}{\sin\varphi} \quad (63)$$

$$F^{\perp}(\varphi) = -\kappa_0 r_0 \ . \quad (64)$$

Notice that these forces have exactly the same structure as in Example A(iii) above, but with a symmetric torque function as in the standard case A(i).

- *(iii)* For asymmetric binding as in Example A(iii) but with angle dependent force we analogously obtain

$$\Omega(\varphi) = -\frac{\kappa_0}{2} d \left\{ \frac{(4 + r_0(1-\cos\varphi)^2) \cdot \cos\varphi - 1}{\sin^2\varphi} + 2(1+r_0) + r_0\cos\varphi \right\} \quad (65)$$

and

$$F^{\parallel}(\varphi) = -\frac{\kappa_0}{\sin\varphi} \left\{ (1 + r_0 - \frac{3}{4} r_0 \cos\varphi)(1-\cos\varphi) + \frac{r_0}{4}\sin^2\varphi \right\} \quad (66)$$

$$F^{\perp}(\varphi) = -\kappa_0 \left\{ 1 + \frac{5}{4} r_0 - \frac{r_0}{2}\cos\varphi \right\} . \quad (67)$$

One can show that both force functions $F^{\parallel}$ and $F^{\perp}$ are negative and monotone decreasing in the variable φ, see Fig. 6b.

According to the plots in Fig. 6b this last Example B(iii) modeling myosin action between the two filaments, shows qualitatively the same behavior as the Example A(iii) with the same cross-linker binding strength function, namely preferred polar binding in direction of the oriented filaments. Indeed, the asymptotic coefficients are a bit larger and produce an even more rapid convergence during antiparallel alignment and a stronger sliding effect near antiparallel alignment (see Fig. 7). Thus, the additional assumption of angle-dependent cross-linker force in (27) for Examples B strengthens the asymmetric convergence behavior, which obviously is induced already by the assumed asymmetric cross-linker binding. Again, with additional stochastic noise introduced in the following section, these effects will become more prominent.

4 Stochastic dynamics

So far the dynamic action of the cross-links was modeled in a mean field approximation, where with an assumed constant reservoir of cross-linking dimers in solution the energy integral kernel $h_\varphi(\rho,\alpha) = \frac{\rho}{\sin\varphi} h(\rho,\alpha,\tilde{\alpha})$ according to (5) measured the mean expected density distribution of bound cross-linkers with respect to their length (ρ) and binding angle (α). Moreover, according to (36) the density of mean force locally exerted by cross-linkers onto one filament could

be expressed by the kernel $K_\varphi(\rho,\alpha) = -\frac{\rho}{\sin\varphi}\partial_\rho h(\rho,\alpha,\tilde\alpha)\cdot\zeta(\alpha)$. Regarding that molecular association and dissociation of cross-linkers are Poisson processes, then also the expected variance will be locally distributed as proportional to h_φ. Thus, for any given intersection angle φ there is a constant b_f measuring the noise amplitude (depending on temperature), so that per infinitesimally small time step dt the *local impulse increment density induced by cross-linkers*, usually given by $d_tP = K_\varphi\,dt$, can now be written as a sum $d_tP = K_\varphi^{det}\,dt + K_\varphi^{stoch}\,dW_t$ with a deterministic increment dt and a stochastic Wiener increment dW_t:

$$d_tP(s,\tilde s)\,ds\,d\tilde s = \left(-\partial_\rho h\frac{\rho}{\sin\varphi}\,dt + b_f\sqrt{h\frac{\rho}{\sin\varphi}}\,dW_t\right)\,d\rho\,d\alpha\cdot\zeta\ . \tag{68}$$

Then, computing the total impulse increment $d_t\mathbf{P} = \mathbf{K}^{det}\,dt + \mathbf{K}^{stoch}\,dW_t$ according to the first integral representation in (40) we obtain stochastic integrals for each of the two force components of $\mathbf{K} = F^\parallel\theta + F^\perp\theta^\perp$ with the following properties:

Proposition 4 (Stochastic differential equations for filament motion) In the situation of Proposition 3, with stochastic noise introduced as described above, instead of (47)–(49) we obtain a system of degenerate stochastic differential equations (for any 2π-periodic φ)

$$d\varphi = \lambda_{\circlearrowleft}\left(\operatorname{sign}(\sin\varphi)\,\Omega_{det}(\varphi)\,dt + b_{\circlearrowleft}(\varphi)|\sin\varphi|^{-\frac{3}{2}}\,dW_t\right)\ , \tag{69}$$

$$ds = \lambda_\parallel\left(F^\parallel_{det}(\varphi)\,dt + b_\parallel(\varphi)|\sin\varphi|^{-\frac{1}{2}}\,dW_t\right)\ , \tag{70}$$

$$ds^\perp = \lambda_\perp\left(\operatorname{sign}(\sin\varphi)\,F^\perp_{det}(\varphi)\,dt + b_\perp(\varphi)|\sin\varphi|^{-\frac{1}{2}}\,dW_t\right)\ . \tag{71}$$

Here the deterministic parts of torque and translation forces are given by the integrals defined in (43)–(45), or by the computed formulas in Examples A and B of section 3 (as they are given for positive φ only). Moreover, the relative noise coefficients $b_\#(\varphi)$ depend continuously on $\cos\varphi$ and $\sin\varphi$, satisfying analogous integral representations for the variances of the stochastic torque and force components

$$b^2_{\circlearrowleft} = |\sin\varphi|^3\,\mathrm{Var}(\Omega_{\mathrm{stoch}}) = b_f^2\int_0^{2\pi}\int_d^\infty |h(\rho,\alpha,\tilde\alpha)|\rho^3 d\rho\,(\sin\alpha\sin\tilde\alpha)^2 d\tilde\alpha \tag{72}$$

$$b^2_\parallel = |\sin\varphi|\,\mathrm{Var}(F^\parallel_{\mathrm{stoch}}) = b_f^2\int_0^{2\pi}\int_d^\infty |h(\rho,\alpha,\tilde\alpha)|\,\rho d\rho\,\cos^2\alpha\,d\alpha \tag{73}$$

$$b^2_\perp = |\sin\varphi|\,\mathrm{Var}(F^\perp_{\mathrm{stoch}}) = b_f^2\int_0^{2\pi}\int_d^\infty |h(\rho,\alpha,\tilde\alpha)|\,\rho d\rho\,\sin^2\alpha\,d\alpha\,. \tag{74}$$

Since the deterministic non-linearities degenerate like $\Omega_{det}\sim|\sin\varphi|^{-2}$ and $F^\#_{det}\sim|\sin\varphi|^{-1}$, the stochastic increments in eqs. (69)–(71) degenerate at a lower order. In particular, using the same notation as for the asymptotic deterministic equation (15), near the singularities $\varphi_* = 0$ and π the leading stochastic equation (69) can asymptotically be written as

$$dy = -a\cdot|y|^{-m}\,dt + b\cdot|y|^{\gamma-m}\,dW_t \tag{75}$$

with $m = 2$ and $\gamma = \frac{1}{2}$. This class of degenerate SDEs does not always lead to well defined stationary processes:

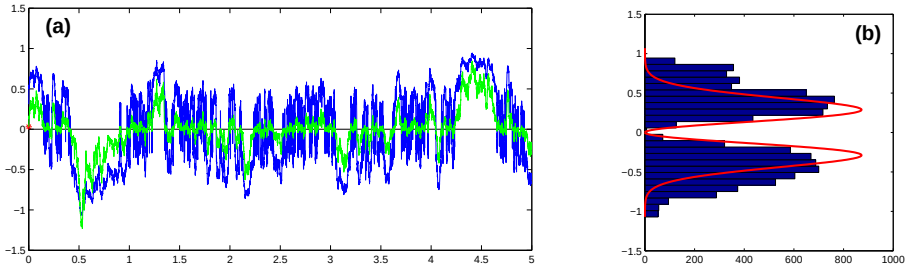

Figure 8: Properties of the asymptotic process y_t for the stochastic variable $\sin \Phi_t$ satisfying (75) with $\gamma = \frac{1}{2}$ and $m = 2$. (a) Stochastic path (black) together with the path of the transformed variable $z_t = y_t^3$ (grey), usually of lower absolute value; (b) empirical distribution of the y_t values (histogram) and theoretical probability distribution according to (76): $p(y) = 2\nu\sqrt{\nu/\pi}\, y^2 \exp(-\nu\, y^2)$ with $\nu = a/b^2$, here $a = 1$ and $b = 0.3$.

Lemma 2 (Resolving power law singularities in SDEs)
The degenerate SDE in (75) with $m > 0$ describes a nontrivial generalized Gauss process that is asymptotically stationary only if the exponents satisfy the condition $0 < \gamma < \frac{m+1}{2}$. The stationary process has the symmetric bimodal probability distribution

$$p(y)\, dy = p_m \cdot |y|^m e^{-\frac{2a}{\mu b^2}|y|^\mu}\, dy \tag{76}$$

with $\mu = m + 1 - 2\gamma > 0$ and a positive scaling factor p_m, see Fig. 8b. Realizations of the stationary process randomly switch between positive and negative values, with super-exponentially long switching intervals ('resting times') and intermittent phases of very fast oscillations, see Fig. 8a.

Proof: Consider the transformed stochastic variable $z = \mathrm{sign}(y)|y|^{m+1}$ satisfying the following non-continuous SDE, with a right-hand side that performs a negative jump at zero, a so-called *'negative sign-type' SDE:*

$$dz = -(m+1)a \cdot \mathrm{sign}(z)\, dt + (m+1)b \cdot |z|^\beta\, dW_t \tag{77}$$

with $\beta = \frac{\gamma}{m+1} > 0$. Computation of the Kolmogorov forward equation reveals that (77) possesses stationary solutions only if $\beta < 1/2$, with symmetric unimodal stationary distribution $p(z) \sim \exp(-\nu|z|^{1-2\beta})$, where $\nu = a/\left((m+1)(\frac{1}{2} - \beta)b^2\right)$. While the deterministic solution without noise consists of straight lines reaching the *absorbing state* zero in finite time, the stochastic realizations show weighted random increments with sufficiently strong perturbations of amplitude $|z|^\beta > \sqrt{z}$, which are able to drive the solution away from

zero, fast enough to overcome the deterministic absorption. □

Applying the results of Lemma 2 to the original asymptotic differential equation (75) for the stochastic variable $y_t = \sin \Phi_t$, satisfying the condition $0 < \gamma = \frac{1}{2} < \frac{3}{2} = \frac{m+1}{2}$ for $m = 2$, we conclude that the stochastic perturbations of order $|\sin \varphi|^{-\frac{3}{2}}$ in (69) are not too strong, but strong enough to overcome the infinitely fast 'attraction' to zero by the deterministic term $d\varphi/dt \sim |\sin \varphi|^{-2}$ and to induce a bimodal stationary distribution, see the stochastic realization in Fig. 8. Interpreted in terms of the biophysical model, this asymptotic result says that the more cross-linkers are active to attract the two filaments towards alignment, with infinitely increasing speed for $\sin \Phi_t \to 0$, the more fluctuations of the stochastic binding process occur and disturb the attraction, strongly enough to prevent complete alignment. Instead, the intersection angle between the two filaments steadily fluctuates around zero, not in a Gaussian manner as for regularly stable steady states, but with a generalized biomodal Gauss distribution so that too small angles are avoided.

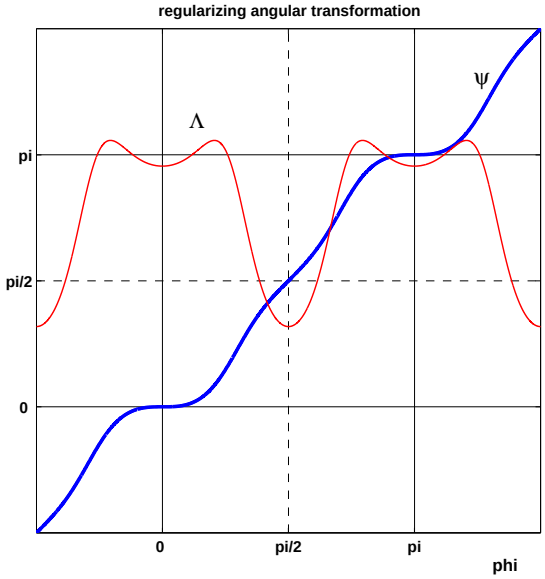

Figure 9: The regularizing periodic transformation $\psi = \psi(\varphi)$ defined in (78) and the positive factor $\Lambda(\psi)$ appearing in the SDE (79), plotted as a function of φ with $\lambda_{\circlearrowleft} = 1$.

As a matter of luck and surprise, we even can find an explicit resolution of the singularities for the 2π-periodic stochastic angle variable Φ_t satisfying the degenerate SDE (69), namely by transforming it into the 2π-periodic variable

$\Psi_t = \psi(\Phi_t)$ according to

$$\psi(\varphi) = \arctan\left\{\frac{\sin^3\varphi}{\cos\varphi}\right\}, \tag{78}$$

satisfying the *'negative sign-type' SDE*

$$d\psi = \Lambda(\psi)\left(-\operatorname{sign}(\sin\psi)\,\omega(\psi)\,dt + b_{\circlearrowleft}(\varphi)|\sin\varphi|^{\frac{1}{2}}\,dW_t\right). \tag{79}$$

All the appearing parameter functions are bounded, particularly the 'regularized' deterministic torque $\omega(\psi) = \Omega_{det}(\varphi)\,\sin^2\varphi$ and the positive function $\Lambda(\psi) = \lambda_{\circlearrowleft}(\cos^2\psi)(3+\tan^2\varphi)$, where also the inverse transformation of (78) can be explicitly calculated as

$$\varphi(\psi) = \arctan\left\{u_+(\tan\psi) + u_-(\tan\psi) + \frac{\tan\psi}{3}\right\}, \tag{80}$$

$$u_\pm(T) = \left\{v(T) \pm \sqrt{v(T)^2 - \left(\frac{T^2}{9}\right)^3}\right\}^{\frac{1}{3}}, \tag{81}$$

$$v(T) = T\,\left(\frac{1}{2} + \frac{T^2}{27}\right). \tag{82}$$

Indeed, (78) is equivalent to a cubic equation for $\Theta = \tan\varphi$, namely $\Theta^3 = (1+\Theta^2)\tan\psi$, whose appropriate solution branch is constructed above. Moreover, whereas at $\varphi \equiv 0 \mod(\pi)$ the transformation $\psi(\varphi) \sim z \sim y^3 \sim \sin^3\varphi$ locally resolves the singularity just as $z = z(y)$ does, see (15) and (77), at $\varphi \equiv \frac{\pi}{2} \mod(\pi)$ the derivative fulfills $\psi'(\varphi) = 1$, so that in a wide region between the singularities ψ resembles the identical mapping, see Fig. 9.

Numerical solutions of the transformed 'negative sign-type' SDEs (77) and (79) with 'negatively jumping' right hand side at $z = 0$ or $\psi \equiv 0 \mod(\pi)$, respectively, can now easily be performed by using the Euler-Marayuma discretization scheme, see [11]. We choose a sufficiently small constant step size, but apply an additional 'freezing' condition for the deterministic increment step, namely $z_{det}(t+dt) = \epsilon \cdot z(t) \approx 0$ if $-dz_{det}/z(t) > dt$, simulating the deterministic absorption at the singularity, while the stochastic increment is added without restriction. Plots of resulting stochastic simulations in terms of the back-transformed solution path for the original degenerate SDEs (75) and (69) are shown in Figs. 8a and 10a, respectively.

Starting the simulated process near one of the stable singularities $\varphi \equiv 0 \mod(\pi)$, then, for a suitable small noise amplitude b_f in the defining equation for the stochastic torque term (72), the transformed angle Ψ_t, thus also the intersection angle Φ_t itself, very rarely leaves the attraction domain of this singular point, so that the distribution of resulting angles resembles that of the localized variable y_t, compare Figs. 8b and 10b. On the other hand, for larger noise amplitudes

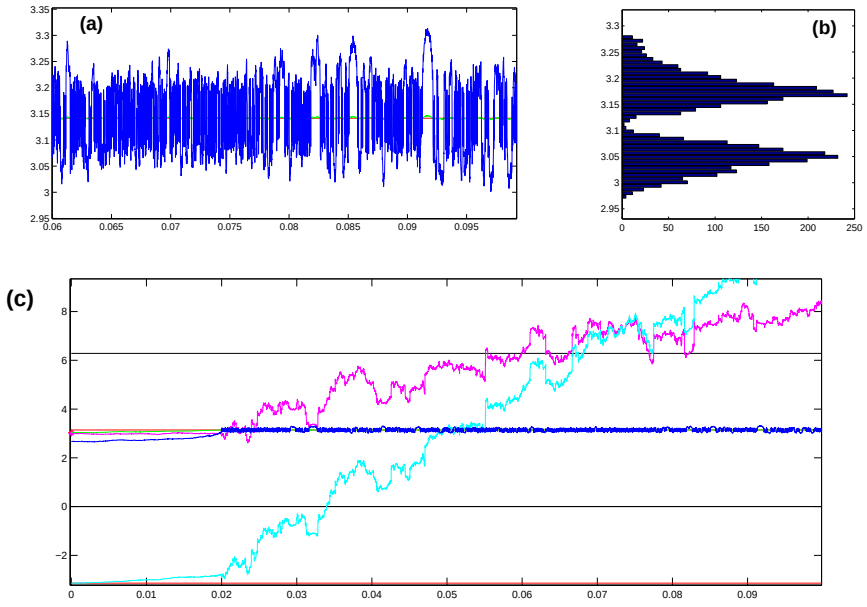

Figure 10: Properties of the stochastic intersection angle dynamics Φ_t satisfying (69) for Example A(iii) with the same parameters as in Fig. 7b and with equal noise coefficients $b_\# = 0.5$ (time step had been chosen as $dt = 0.0005$). (a) The stochastic path (black) is part of the longer time series in (c) during the stationary phase of small fluctuations around π; (b) empirical distribution of the Φ_t values for the stationary phase; (c) longer time series of the intersection angle Φ_t (black with tiny fluctuations) together with the other two stochastic variables determining the position of the moving filament, namely the section length S_t (upper curve) and the x-value of the intersection point with the fixed filament R_t (lower curve). The corresponding visualization of filament motion is depicted below in Fig. 12a and supplementary Movie A12.

b_f the stochastic angular path can switch from one singularity to the other, depending on its stability measured by the value of $\omega(\cos\varphi, \sin\varphi)$ for $\cos\varphi = \pm 1$.

Finally, let us apply the so far performed asymptotic and numerical analysis to the full degenerate SDE system in (69)–(71) in order to visualize and interpret the resulting dynamics of interactive filament motion. For this we have to stochastically and numerically solve the 'just integrating' degenerate SDEs for s_t and $s_t^\perp$, (70) and (71), which have additive Gaussian increments with noise amplitude proportional to $|\sin\Phi_t|^{-\frac{1}{2}}$. Therefore the variance of these stochastic increments is bounded by the expectation value $\mathcal{E}(|\sin\Phi_t|^{-1}) = \mathcal{O}\left(1 + \mathcal{E}(|y_t|^{-1})\right) < \infty$, because with the aid of (76) the probability distribution for the well-defined inverse process $u_t = (y_t)^{-1}$ can easily be calculated as $p(u) \sim u^{-4}\exp(-\nu\, u^{-2})$ having finite mean value and variance. Thus, also the stochastic process $\Sigma_t = (\sin\Phi_t)^{-1}$ is a well defined generalized Gaussian

process so that, for example, the SDE for s_t in (70) is of the type

$$ds_t = a(\Phi_t) \cdot |\Sigma_t|\, dt + b(\Phi_t) \cdot \sqrt{|\Sigma_t|}\, dW_t\,, \tag{83}$$

being integrable and resulting in non-stationary stochastic solutions s_t. The same is valid for solutions $s_t^\perp$ of (71). Numerically, these two stochastic differential equations are simultaneously solved together with the solution of the degenerate SDE (79) for Ψ_t, again using the Euler-Marayuma method, where also the deterministic increments ds_{det} and $ds_{det}^\perp$ are locked into the 'freezing' condition for the variable Ψ_t. Notice that near the singularities we have $|\Sigma_t| \sim |\Psi_t|^{-\frac{1}{3}}$.

We can then visualize the stochastic motion of filament Γ with respect to the fixed filament $\widetilde{\Gamma}$ by using the equations in (50) and calculating the increments of the defining variables S_t and R_t in analogy to eqs. (52)–(53), namely

$$dS_t = ds_t + \Sigma_t \cdot \cos\Phi_t\, ds_t^\perp\,, \tag{84}$$

$$dR_t = -\Sigma_t\, ds_t^\perp\,. \tag{85}$$

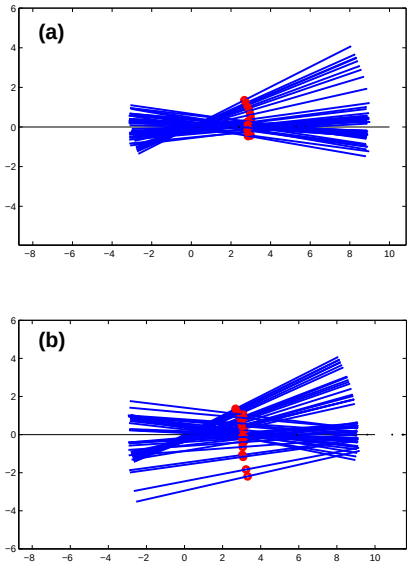

Figure 11: Plots of the stochastic filament dynamics for Examples (a) A(iii) and (b) B(iii), where the intersection angle $\Phi(t)$ fluctuates around the parallel steady state 0. Parameters in the SDEs (69),(84),(85) are $\lambda_{\circlearrowleft} = 1$, $\lambda_\perp/2 = \lambda_\parallel = 1.5$ and equal noise amplitudes $b_\# = 0.1$. In contrast to the deterministic situation in Fig. 7, the sequence of the moving filament (for simplicity drawn with finite length) is plotted for fixed time intervals of length $dtplot = 200 \cdot dt$ with $dt = 0.00001$. The whole simulation period is 0.1 time units. See also the supplementary Movies A11 and B11.

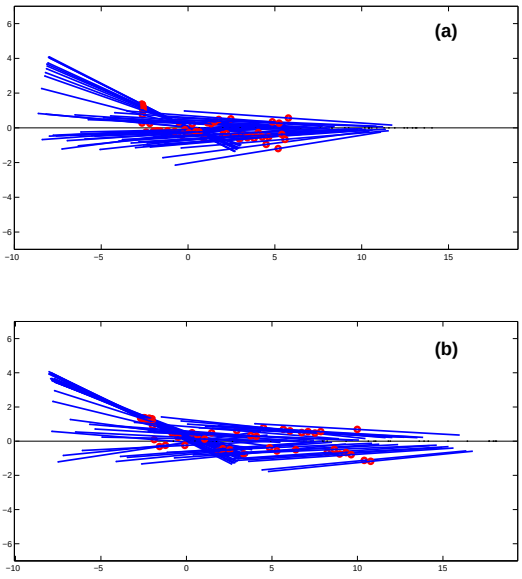

Figure 12: Plots of the stochastic filament dynamics for Examples (a) A(iii) and (b) B(iii) as in Fig. 11, but now with fluctuations around the anti-parallel steady state π, see also the Movies A12 and B12.

The pictures in Figs. 11 and 12 certify the asymptotic results obtained in the deterministic case and show that the effects already seen in Fig. 7 are clearly amplified by introducing the weighted degenerate noise terms.
In particular, the stochastic fluctuations around *parallel alignment* reveal slight rotations of the filament without any translations parallel to the fixed filament: for Example A(iii) see Fig. 11a in comparison with Fig. 7b, and for Example B(iii) Fig. 11b in comparison with Fig. 7d, where the slight orthogonal drift in the deterministic case obviously corresponds to stronger random drifts in the stochastic case.
Analogously, during *antiparallel alignment* the stochastic motion of the filament again reveals slight rotations, but now superimposed by a steady parallel sliding drift to the right, which is less expressed in Example A(iii), see Fig. 12a and its deterministic counterpart Fig. 7a, as compared to the stronger sliding in Example B(iii), see Fig. 12b and its counterpart Fig. 7c.

Though these stochastic model simulations are performed for the idealized situation of two infinitely long stiff filaments, the asymptotic behavior around the singular states of parallel and antiparallel alignment already reproduce the characteristic phenomenon of actin filament sliding, as it is experimentally observed and functionally effective in muscle contraction and cellular stress fibers: When an extensive pool of phosphorylated myosin dimers can cross-link two long actin filaments, they induce active sliding if and only if the two filaments are overlapping and oppositely oriented; then their filament tips (with the so-called

'barbed ends' anchored in the Z-lines or the plasma membrane) move towards each other so that, for instance, in a muscle cell the sarcomeres can eventually be contracted. The reason is that, as the model assumptions suppose, myosin dimers preferentially bind to an actin filament with its head oriented towards the 'barbed end', see the model in Example A(iii) and Fig. 5b, and that under this condition they can also perform a stochastic power-stroke inducing a pre-tension of their elastic 'springs' (between head and tail), see the additional model assumptions in Example B(iii) and Fig. 5c.

We emphasize the difference between this 'active' dynamics and the simple negative gradient flow dynamics as shown by the symmetric model A(i). There, also during stochastic motion of a filament pair, the mutual interaction energy always tends to the (infinitely negative) energy minimum of alignment. In contrast, for the asymmetric 'myosin-like' models A(iii) and B(iii) the additional energy, which is fed into the filament pair system due to preferential binding and hydrolysis-mediated active force application by the cross-linkers, induces the additional phenomenon of angle-dependent filament sliding, an 'active' effect that is superimposed onto the simple physical law of energy minimization.

As already mentioned in section 2, Fig. 2, the trace C_d of all possible cross-linker states of minimal length is an ellipse along one of the diagonals $\{s = \tilde{s}\} or \{s = -\tilde{s}\}$, increasing in size proportionally to $1/|\sin\varphi|$ as the intersection angle $|\varphi|$ or $|\pi - \varphi|$ between the filaments becomes smaller. This means nothing else than that, in the same manner, the filament part carrying bound cross-links increases in size. However, due to the model assumptions above, with the amount of active cross-linkers also the variance of induced 'molecular noise' likewise increases, so that the resulting stationary stochastic process shows a vanishing probability of 'true' alignment. More precisely, as can be seen in the asymptotic histogram in Fig. 10b, small intersection angles very rarely occur, but there is a clear hump around a positive mean absolute angular deviation, which can be explicitly computed, with a finite expected value for the inverse sine, namely $\mathcal{E}(|\sin\Phi_t|^{-1}) < \infty$. This has the important consequence that also the mean number of active cross-linkers and the mean interval length of occupied binding sites on each filament stay finite during the fluctuating alignment process.

Thus, although the hypothesis of infinite filament length, which has been supposed for the current model, induces a degenerate convergence of the deterministic dynamics to complete alignment along the whole infinite filaments in finite time, the implementation of an appropriately modeled and scaled stochastic noise reverses this extreme behavior near the singularity and makes very small intersection angles very rare, so that most of the time only finite parts of the filaments are connected by cross-linkers.

Nevertheless, for applying these model results to biopolymer dynamics, the

additional effects due to finite filament length should be investigated, which is briefly undertaken in the following last section.

5 Dynamics of a filament with finite length

In order to explore the effects due to a more realistic modeling of semi-flexible filaments as stiff rods having finite length, we consider the simplified situation of pairing a short filament with a relatively long filament. Therefore, we could assume that the longer filament stays fixed and that the smaller filament performs its 'interaction dance' on the middle part of this fixed filament, thereby not reaching its ends. Consequently, the fixed filament can be supposed as infinitely long.

Under these conditions the forgoing model equations in section 3 have just to be adapted in order to calculate torque and translation forces onto the moving filament Γ. Again supposing that only the spring forces of cross-linkers come into action, then under the simplifying assumption made in Example B, namely that the cross-link length is approximately constant, $\rho \equiv d$, the measure valued version of the local force kernel $K_f = K(s, \tilde{s})$ can be used as it appears in (40) and (31). However, the integration domain in the $(s, \tilde{s})$-space is now restricted to those parts of the ellipse C_d whose s-values lie on the filament, see Fig. 2. Let us remind that s denotes the arc length on filament Γ with $s = 0$ representing the intersection point with the other filament. Choosing the *mass center* as fixed point $(X(t), Y(t))$ on the moving filament, then according to the terminology in (50) the variable $S = S(t)$ denotes the s-value of this center point, so that with finite filament length L the condition for s to represent an arbitrary point on the filament is

$$|s - S| \leq \frac{L}{2}\,. \tag{86}$$

Since the integration in all torque and force integrals is performed only on the curve C_d, the relevant s-values representing occupied cross-link binding sites, see (4), satisfy

$$|s| = |\frac{d \cdot \sin(\varphi + \alpha)}{\sin \varphi}| \leq \frac{d}{\sin \varphi}\,, \tag{87}$$

where we again restrict the derivation of this formula to the case $0 < \varphi < \pi$. For all these s-positions except the extreme ones, there are two angles α and $\hat{\alpha} = \pi - 2\varphi - \alpha$, under which cross-linkers can bind, see Figs. 1 and 2. Then the twofold integration domain is given by the intersection of both conditions (86) and (87) yielding $s_-(\varphi, S) \leq s \leq s_+(\varphi, S)$ with

$$s_\pm(\varphi, S) = \pm \min(\frac{d}{\sin \varphi}, \frac{L}{2} \pm S)\,. \tag{88}$$

Transformation into the α-parametrization, using the property

$$ds = \cos(\varphi + \alpha)\, \frac{d}{\sin \varphi}\, d\alpha \tag{89}$$

gives a well-determined integration domain $\{\alpha \in A_{\varphi,S}\}$ and a 'symmetry-map' $\alpha \mapsto \hat{\alpha}$ with the property $\sin(\varphi + \hat{\alpha}) = \sin(\varphi + \alpha)$, so that both angles belong to the same binding site s and that any of the integral representations with a kernel $g = g_\varphi(\alpha)$ as in eqs. (43)–(45) can be written as a twofold integral over s, expressed by the sum of two integrands, namely $g_\varphi(\alpha)$ and $g_\varphi(\hat{\alpha})$:

$$\begin{aligned} \frac{d}{\sin\varphi} \int_{A_{\varphi,S}} g_\varphi(\alpha)\, d\alpha &= \int_{s_-(\varphi,S)}^{s_+(\varphi,S)} \frac{g_\varphi(\alpha) + g_\varphi(\hat{\alpha})}{\cos(\varphi+\alpha)}\, ds \\ &= \frac{d}{\sin\varphi} \int_{r_-(\varphi,S)}^{r_+(\varphi,S)} \frac{g_\varphi(\alpha) + g_\varphi(\hat{\alpha})}{\sqrt{1-r^2}}\, dr\,. \end{aligned} \tag{90}$$

In the last integral transformation we have used the substitution of s in (4) by the 'normalized' variable

$$r = \sin(\varphi + \alpha) = \frac{\sin\varphi}{d}\, s \tag{91}$$

with integration domain limited by

$$r_+(\varphi, S) = \min\left\{1, \frac{\sin\varphi}{d}\left(S + \frac{L}{2}\right)\right\} \tag{92}$$

$$r_-(\varphi, S) = \max\left\{-1, \frac{\sin\varphi}{d}\left(S - \frac{L}{2}\right)\right\}. \tag{93}$$

In dependence of the occurring angles α, $\tilde{\alpha} = \pi - \varphi - \alpha$ and $\hat{\alpha} = \pi - 2\varphi - \alpha$ with the properties $\widetilde{\tilde{\alpha}} = \alpha + \varphi$ and $\widehat{\tilde{\alpha}} = \alpha - \varphi$ we can state the following formulas for the trigonometric functions, by using the subsidiary function $Q_r := \sqrt{1-r^2}$,

$$\begin{aligned} \sin\tilde{\alpha} &= \sin\tilde{\hat{\alpha}} = r \\ \cos\tilde{\alpha} &= -\cos\tilde{\hat{\alpha}} = -Q_r \\ \sin\alpha &= r\cos\varphi - Q_r \sin\varphi\,; \quad \cos\alpha = r\sin\varphi + Q_r\cos\varphi \\ \sin\hat{\alpha} &= r\cos\varphi + Q_r \sin\varphi\,; \quad \cos\hat{\alpha} = r\sin\varphi - Q_r\cos\varphi\,. \end{aligned}$$

With the aid of these formulas the integral in (90) over r for any of the torque and force representations in section 3 can be explicitly calculated in terms of the integration limits. For computing the torque, for instance, in the case of infinitely long filaments the virtual rotation was performed around the intersection point, which now has to be replaced by the mass center. Thus, using a generalized version of (41) provides the following integral representation for the total torque onto filament Γ:

$$\begin{aligned} \Omega(\varphi, S) &= \int_\Gamma \int_{\widetilde{\Gamma}} (s - S)\; \theta^\perp \cdot K_f\, d\tilde{s}\; ds \\ &= \frac{\bar{h}/2\pi}{\sin\varphi} \int_{A_{\varphi,S}} k_\varphi(\alpha) \left(\frac{d}{\sin\varphi}\sin\tilde{\alpha} - S\right) \sin\alpha\; q(\tilde{\alpha})\, q(\alpha)\, d\alpha\,. \end{aligned} \tag{94}$$

Similar representations can be obtained for the forces $F^\parallel$ and $F^\perp$.

Let us define the second auxiliary function $G_r = \frac{1}{\pi}\left(\arcsin(r) - r\ Q_r\right)$, being an odd function on the maximal integration interval $[-1,1]$ with infinite slope at $r = \pm 1$ and flat asymptotics $G_r \sim \frac{2}{3\pi} r^3$ near $r = 0$. Then we obtain for

Example A(i) with infinitely stiff cross-linkers:

$$\begin{aligned}
\Omega(\varphi, S) &= -2\kappa_0 \frac{\cos\varphi}{\sin\varphi}\left(\frac{d}{\sin\varphi}\frac{1}{2}[G_{r_+(\varphi,S)} - G_{r_-(\varphi,S)}] - \frac{S}{\pi}[Q_{r_-(\varphi,S)} - Q_{r_+(\varphi,S)}]\right), \\
F^{\parallel}(\varphi, S) &= -\frac{2\kappa_0}{\pi}[Q_{r_-(\varphi,S)} - Q_{r_+(\varphi,S)}], \\
F^{\perp}(\varphi, S) &= -\frac{2\kappa_0}{\pi}\frac{1}{\tan\varphi}[Q_{r_-(\varphi,S)} - Q_{r_+(\varphi,S)}].
\end{aligned}$$

In general, the ODEs for the three dynamic variables $\Phi(t)$, $S(t)$ and $R(t)$ can be taken as in (51)–(53), now with the nonlinearities also depending on $S(t)$ and, clearly, on the length L of the filament (including the inverse friction coefficients). The consequence is that now the first two differential equations constitute a nonlinearly coupled ODE system:

$$\frac{d\Phi}{dt} = \lambda_{\circlearrowleft}\ \Omega(\Phi, S), \tag{95}$$

$$\frac{dS}{dt} = \lambda\ F_S(\Phi, S) := \lambda_{\parallel}\ F^{\parallel}(\Phi, S) + \frac{\lambda_{\perp}}{\tan\Phi}\ F^{\perp}(\Phi, S). \tag{96}$$

The corresponding plots of the torque $\Omega(\varphi, S)$ and 'shift force' $F_S(\varphi, S)$ are depicted in Fig. 13. A nonzero shift force does only appear for larger values of $|S|$ and small intersection angles (Fig. 13b), when cross-linkers only 'pull' at one side of the finite filament. For discussing the more complex plot of the torque (Fig. 13a), we show its contour map in Fig. 14a and the section profile at $S = 0$ in Fig. 14b. The latter shows, that pure rotational motion of the finite filament behaves similar as shown in section 3, see Fig. 4a, but only as long as the intersection angle is so large that the binding sites of active cross-linkers lie on the interior of the filament, namely $L \cdot |\sin\Phi| > 2d$. As soon as the angle gets smaller, less cross-link combinations are possible and the torque drastically falls to zero, but still linearly for $\sin\phi \to 0$:

$$\begin{aligned}
\Omega(\varphi, 0) &\sim -\operatorname{sign}(\sin\varphi)\frac{\cos\varphi}{\sin^2\varphi}\ \min\{1, G_{L\cdot|\sin\varphi|/2d}\} \\
&\sim -\left(\frac{L}{d}\right)^3 \cos\varphi \cdot \sin\varphi\,.
\end{aligned}$$

This means that, due to the finite filament length, the two alignment states $\varphi_* = 0$ and π are no longer singular points for the filament dynamics, they rather are regular asymptotically stable equilibria. Translated into the local analysis of the preceding sections, the corresponding 'sign-type' degenerate ODEs for z_t or Ψ_t are now smoothed in a specific manner, which is just induced by the model formulation for cross-link action.

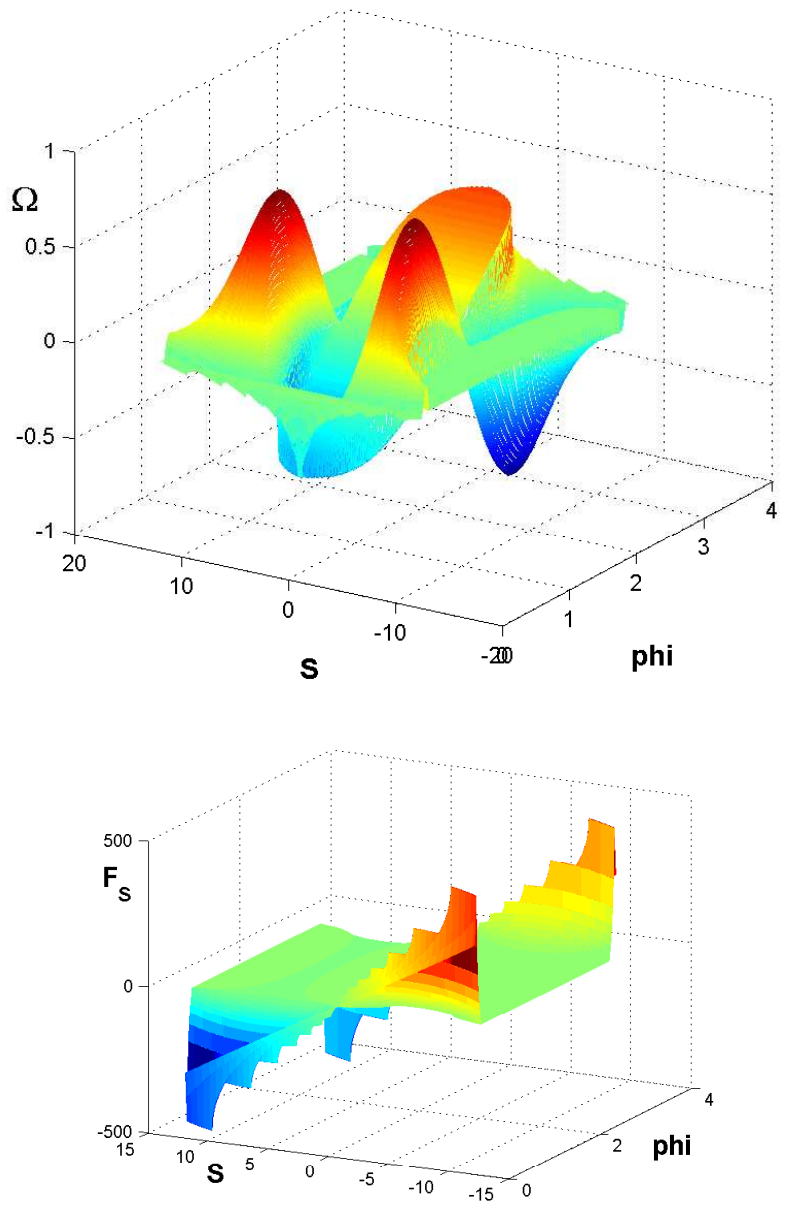

Figure 13: (a: upper picture) The torque $\Omega(\varphi, S)$ and (b: lower picture) the 'shift force' $F_S(\varphi, S)$ for a finite moving filament of length $L = 12$ with cross-link length $d = 1$ using the model of the standard Example A(i). Parameters are as in Fig. 7b.

The changed filament dynamics due to finite length becomes even more prominent, when the fixed filament is intersected by the moving one only for a small part at its rear end, since then $S(t) \gg 0$. As can be seen in Fig. 15 (and also in Fig. 14a, where the $(\Phi(t), S(t))$ trajectory is plotted into the contour dia-

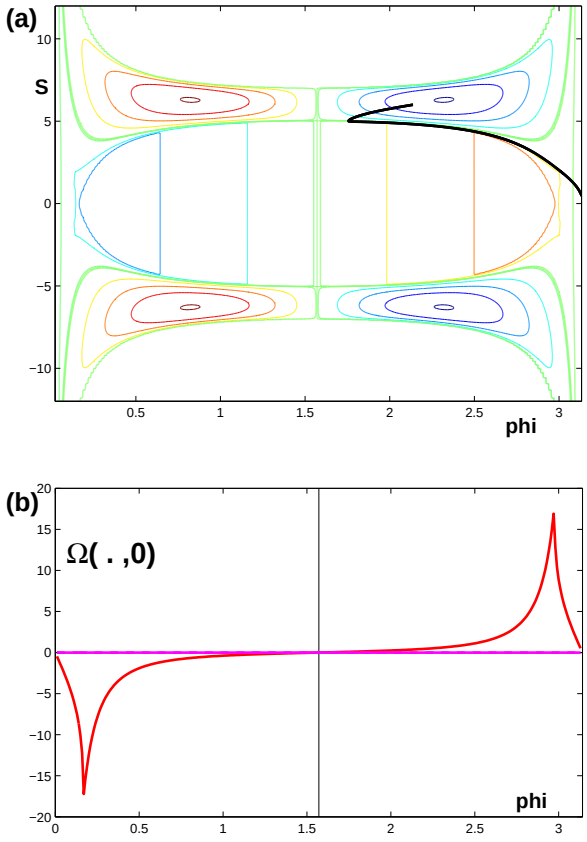

Figure 14: (a) Contour lines of the torque $\Omega(\varphi, S)$ together with a specific trajectory of eqs. (95)–(96), and (b) profile of $\Omega(\varphi, 0)$ for the situation when the intersection point is the mass center of the moving filament, see the text for comparison with the corresponding plot in Fig. 4a.

gram) the filament is slowly pulled towards the fixed filament, with $S(t)$ slowly decreasing, but first the intersection angle gets wider, before finally the rapid rotational movement towards antiparallel alignment takes place. In spite of the regularized singularity as discussed above, the trajectory very rapidly reaches the asymptotic alignment state because of a very fast exponential decay.

Finally, most interesting is a combination of the results in sections 4 and 5, namely when implementing stochastic perturbations into the ODE-system (95)–(96) by explicitly computing the corresponding noise amplitudes $b_{\#}(\varphi, S)$ in analogy to (72)–(74). The properties of this full SDE system is currently explored and promises to reproduce some more interesting phenomena for short filament interaction.

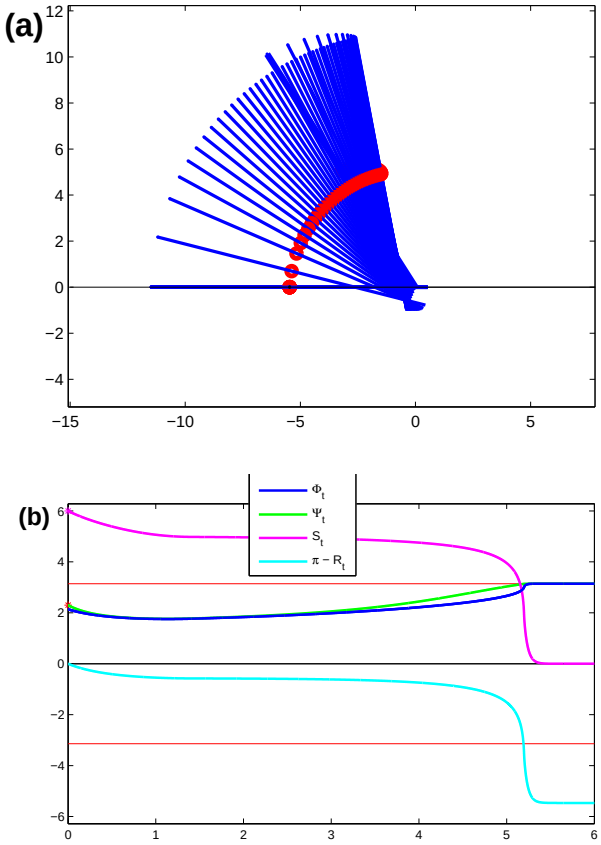

Figure 15: Deterministic dynamics of a finite moving filament on a fixed infinite filament (the x-axis) for model A(i) with parameters and conditions as in Fig. 13. In (a: upper picture) the filament finally aligns antiparallelly, but the intersection angle $\pi - \Phi_t$ first increases towards $\pi/2$ while the filament is pulled down, before the angle rapidly adjusts to alignment, see the dark curve in (b: lower picture) and Movie A15. The convergence of $\Phi_t \to \pi$ as well as of the two other variables S_t and R_t towards a steady state is not performed in finite time: due to the smoothed Ω function (see Fig. 14b) there remain tiny deviations that are exponentially decreasing, though with a fast rate of order $(L/d)^3 = 12^3$ in our case.

6 Summary and further applications

The most important feature of the presented continuum model, for the interaction between stiff filaments, is the possibility to derive explicit local force kernels for a variety of applicable cross-linking mechanisms, which then can be used to calculate torques and translational forces between the 'rods' as explicit global integrals depending only on the geometric constellation. Clearly, this is valid only under the assumed hypothesis that there is a continuum of potential

cross-link binding sites and a pseudo-stationary equilibrium in the Poisson process of binding and unbinding. However, not only the mean binding strength in dependence of the geometric variables is condensed into a deterministic model; also the stochastic fluctuations are modeled and simulated according to an appropriate Gaussian noise kernel in the global integrals. Then, stochastic integration provides explicit variance expressions for the additive stochastic torques and forces, leading to a system of degenerate stochastic differential equations (SDEs) for the filament variables (position and direction).

So far we have restricted the derivation of local force kernels to the case that stiff cross-linkers (as e.g. myosin dimers) apply forces only in direction of their 'connection vector'. However, many cross-linking polymers could be bent or twisted (as filamin, fascin or α-actinin) and thus could exert torque moments onto the attached filaments (see e.g. [24],[18]). Under suitable model assumptions on the type and angular dependence of cross-linker micromechanics, analogous explicit kernels for the corresponding forces (K_ω and $K_{\tilde{\omega}}$ in our notation) can then be derived. Obviously, the resulting degenerate differential equations could have different asymptotics and reveal a variety of other convergence and fluctuation properties.

As one advantage of this simplified model we have demonstrated a thorough asymptotic analysis around the singular states of parallel and antiparallel alignment, from which some basic properties of the stochastic processes can be quantitatively extracted. Moreover, the presented regularization procedures are also used for consistent numerical procedures to simulate the degenerate stochastic dynamics, which reveals typical properties of actin filament sliding in the case that 'contractile' myosin dimers act as cross-linkers.

As a further advantage, the explicitly computable (deterministic and stochastic) integrals could be easily used for more realistic worm-like-chain (WLC) models of longer semi-flexible filaments, if just applied to all possible pair interactions between piecewise straight segments of the discretized filaments. The resulting numerical algorithms, which reflect the approximative pseudo-stationary cross-linking process, could well compete with so far used 'molecular dynamics' simulations that uses multi-particle methods to represent individual cross-linkers (see e.g. [15]), particulary when applied to whole networks of interacting filaments as they currently are observed in experiments, see [1], for instance.

Moreover, for the real 3-dimensional biological system of semi-flexible actin filaments, most of the 2-dimensional dynamic properties presented here can be carried over and used as a basic description for more generalized interaction model: There is an additional degree of freedom not only in filament rotation and bending, but also in parametrizing the space angles of cross-link binding. Finally, we hope that an application of our approach, namely to derive explicit local interaction kernels from detailed molecular mechanisms on a microscale,

could give an input to the improvement or new development of more physiological (than purely phenomenological) continuum models for thermodynamical and fluid dynamical theories of polymer networks (see e.g. [2] or [10]), particularly for modeling and simulating the contractile actin-myosin cytoskeleton in biological cells (see [12]).

Acknowledgement
We thank the DFG for generously supporting this research, particularly within the Special Research Program (SFB 611) on *Singular Phenomena and Scaling in Mathematical Models* at Bonn University.

Supplementary material
Visualization of the stochastic filament dynamics depicted in Figs. 11, 12 and 15 in a form of picture sequences (Movies [A11, B11], [A12, B12] and A15) will be available under `www.theobio.uni-bonn.de\~filaments-stochastic`.

References

[1] P.M. Bendix et al. and D.A. Weitz. A quantitative analysis of contractility in active cytoskeletal protein networks. *Biophys. J.* 94: 3126–3136, 2008.

[2] I. Borukhov, R.F. Bruinsma, W.M. Gelbart and A.J. Liu. Structural polymorphism of the cytoskeleton: a model of linker-assisted filament aggretation. *Proc. Natl. Acad. Sc. USA* 102: 3673–3678, 2005.

[3] S. Blatt and P. Reiter. Does finite knot energy lead to differentiability? Preprint no. 12, Institut für Mathematik, RWTH Aachen 2006; see `http://www.instmath.rwth-aachen.de/` → `preprints`. To appear in *J. Knot Theory Ramifications*.

[4] J. Cantarella, M. Piatek and E. Rawdon. Visualizing the tightening of knots. In: VIS'05: *Proc. of the 16th IEEE Visualization 2005*, pp. 575–582. IEEE Computer Society, Washington, DC, 2005.

[5] M.H. Freedman, Zheng-Xu He and Zhenghan Wang. Möbius energy of knots and unknots. *Ann. of Math.(2)*, 139(1): 1–50, 1994.

[6] O. Gonzalez, J.H. Maddocks, F. Schuricht and H. von der Mosel. Global curvature and self-contact of nonlinearly elastic curves and rods. *Calc. Var. Partial Differential Equations*, 14(1): 29–68, 2002.

[7] Zheng-Xu He. The Euler-Lagrange equation and heat flow for the Möbius energy. *Comm. Pure Appl. Math.*, 53(4): 399–431, 2000.

[8] S. Highsmith. Lever arm model for force generation by actin-myosin-ATP. *Biochemistry* 38: 791-797, 1999.

[9] L.W. Janson and D.L. Taylor. Actin-crosslinking protein regulation of filament movement in motility assays: a theoretical model. *Biophys. J.* 67: 973-982, 1994.

[10] J.F. Joanny, F. Jülicher, K. Kruse and J. Prost. Hydrodynamic theory for multicomponent active polar gels. *New J. Phys.* 9: 422, 2007.

[11] P.E. Kloeden and E. Platen. *Numerical Solution of Stochastic Differential Equations*. Springer, Berlin, 1992.

[12] S.A. Koestler, S. Auinger, M. Vinzenz, K. Rottner and J.V. Small. Differentially oriented populations of actin filaments generated in lamellipodia collaborate in pushing and pausing at the cell front. *Nature Cell Biol.* 10.1038/ncb1692, 2008.

[13] R.B. Kusner and J.M. Sullivan. Möbius-invariant knot energies. In [22], pp. 315–352, 1998.

[14] Xiumei Liu and G.H. Pollack. Stepwise sliding of single actin and myosin filaments. *Biophys. J.* 86: 353-358, 2004.

[15] F. Nédélec. Computer simulations reveal motor properties generating stable antiparallel microtubule interaction. *J. Cell Biol.* 158: 1005–1015, 2002.

[16] J. O'Hara. Energy of a knot. *Topology*, 30(2): 241–247, 1991.

[17] J. O'Hara. *Energy of knots and conformal geometry*. Vol. 33 of: *Series on Knots and Everything*. World Scientific Publishing Co. Inc., River Edge, NJ, 2003.

[18] O. Peletier et al. and C.R. Safinya. Structure of actin cross-linkes with α-actinin: a network of bundels. *Phys. Rev. Letters* 91(14): 148102, 2003.

[19] P. Reiter. *Knotenenergien*. Diploma thesis, Math. Inst. Univ. Bonn, 2004.

[20] P. Reiter. *On repulsive knot energies*. PhD thesis, RWTH Aachen, to appear in Oct. 2008.

[21] F. Schuricht and H. von der Mosel. Characterization of ideal knots. *Calc. Var. Partial Differential Equations* 19: 281–305, 2004.

[22] A. Stasiak, V. Katritch and L.H. Kauffman, editors. *Ideal knots*. Vol. 19 of: *Series on Knots and Everything*. World Scientific Publishing Co. Inc., River Edge, NJ, 1998.

[23] P. Strzelecki and H. von der Mosel. On rectifiable curves with L^p-bounds on global curvature: Self-avoidance, regularity, and minimizing knots. *Math. Z.* 257: 107–130, 2007.

[24] J. Ylänne, K. Scheffzek, P. Young and M. Saraste. Crystal structure of the α-actinin rod reveals an extensive torsional twist. *Structure* 9: 597–604, 2001.